TU Delft

Delft University of Technology

Document Version
Final published version

Licence
CC BY

Citation (APA)
Malschaert, D., Mohabeddine, A., Veljkovic, M., Leonetti, D., & Maljaars, J. (2027). Near-threshold fatigue crack growth rates in heat-affected zone microstructures in weldments of steel structures. *International Journal of Fatigue*, *214*, Article 109904. https://doi.org/10.1016/j.ijfatigue.2026.109904

Important note
To cite this publication, please use the final published version (if applicable).
Please check the document version above.

Copyright
In case the licence states “Dutch Copyright Act (Article 25fa)”, this publication was made available Green Open Access via the TU Delft Institutional Repository pursuant to Dutch Copyright Act (Article 25fa, the Taverne amendment). This provision does not affect copyright ownership.
Unless copyright is transferred by contract or statute, it remains with the copyright holder.

Sharing and reuse
Other than for strictly personal use, it is not permitted to download, forward or distribute the text or part of it, without the consent of the author(s) and/or copyright holder(s), unless the work is under an open content license such as Creative Commons.

Takedown policy
Please contact us and provide details if you believe this document breaches copyrights.
We will remove access to the work immediately and investigate your claim.

This work is downloaded from Delft University of Technology.

International Journal of Fatigue 214 (2027) 109904

Contents lists available at ScienceDirect

International Journal of Fatigue

journal homepage: www.elsevier.com/locate/ijfatigue

Near-threshold fatigue crack growth rates in heat-affected zone microstructures in weldments of steel structures

David Malschaert [a,b,*], Anis Mohabeddine [a], Milan Veljkovic [a], Davide Leonetti [c], Johan Maljaars [c,d]

[a] Department of Engineering Structures, Delft University of Technology, Stevinweg 1, Delft, 2628 CN, The Netherlands
[b] Department of Steel and Movable Structures, Iv-Infra, Waarderweg 40, Haarlem, 2031 BP, The Netherlands
[c] Department of Built Environment, Eindhoven University of Technology, Groene Loper 3, Eindhoven, 5612 AZ, The Netherlands
[d] Department of Structural Reliability, TNO, Molengraaffsingel 8, Delft, 2629 JD, The Netherlands

ARTICLE INFO

Keywords:
Fatigue crack growth
Heat-affected zone
Near-threshold region
CT specimens

ABSTRACT

This study investigates the near-threshold fatigue crack growth behaviour of heat-affected zone (HAZ) microstructures in welded structural steels with nominal yield strength of 235 MPa and 355 MPa. Quantifying the influence of these microstructures is important for reliable assessment of the remaining fatigue life of welded structures. The microstructures of the HAZ subregions were experimentally simulated on material samples representative for bridge structures with a Gleeble thermal-mechanical simulator after which compact tension specimens were extracted. The fatigue crack growth tests were performed with ΔK-decreasing procedure at load ratios of $R = 0.1$ and $R = 0.5$. The crack length was monitored using the alternating current potential drop technique. At $R = 0.1$, the simulated HAZ subregions of both steels exhibited lower crack growth rates and higher long crack threshold stress intensity factors, than their respective base metals. This increased resistance was attributed primarily to enhanced roughness-induced crack closure. At $R = 0.5$, no significant differences were observed between the simulated HAZ subregions and the corresponding base metals, consistent with the suppression of crack closure effects at higher load ratios.

1. Introduction

Field inspections of welded steel bridges constructed between the 1950s–1980s have identified recurring weld defects [1,2], such as cold cracks. Fig. 1 presents an example of a cold crack found in the flange of a main girder of a bridge. Although cold cracks are uncommon in modern construction – due to advances in welding procedures and improvements in the weldability of structural steel grades – they remain a concern in existing bridges from that period. Therefore, the accurate assessment of the fatigue life for these defects is important. Reliable estimations of the fatigue crack growth are crucial to assess remaining service life and to optimise inspection intervals of bridges with such defects.

Structural steels used in bridges during the 1950s–1980s were commonly designed to achieve the required strength through alloying and carbon contents [3,4]. Consequently, these steels exhibited relatively high carbon equivalent values (C_{ev}). During welding, this leads to increased hardness of the heat-affected zone (HAZ), making these steels vulnerable to cold cracks.

Fatigue cracks in weldments of steel structures often extend through the HAZ into the base metal [5]. The cold crack example from Fig. 1 was formed after the tack welding process and the crack followed the coarse grained HAZ (CGHAZ) of the tack weld [6]. The cold crack did not extend during deposition of the subsequent pass over the tack weld, nor during service of the bridge. The main loading direction is indicated in Fig. 1 with respect to the defect. When the crack would propagate from its initial orientation, as a result from cyclic loading, the expected growth path is through the HAZ into the base metal. Consequently, it would cross regions with differing microstructures. Understanding and quantifying how these microstructures influence fatigue crack growth is therefore essential for accurate fatigue life predictions of fatigue cracks in weldments.

The formation of the HAZ heterogeneous microstructure and its mechanical properties depend on numerous factors, including the welding procedure, process parameters, and chemical composition [5]. While the fatigue crack propagation behaviour of long cracks is generally considered to be not influenced by the microstructure [7], several

* Corresponding author at: Department of Engineering Structures, Delft University of Technology, Stevinweg 1, Delft, 2628 CN, The Netherlands.
E-mail address: D.H.Malschaert@tudelft.nl (D. Malschaert).

https://doi.org/10.1016/j.ijfatigue.2026.109904
Received 15 April 2026; Received in revised form 31 July 2026; Accepted 1 August 2026
Available online 6 August 2026
0142-1123/© 2026 The Authors. Published by Elsevier Ltd. This is an open access article under the CC BY license (http://creativecommons.org/licenses/by/4.0/).

Nomenclature

Latin symbols

a	Crack length
a_0	Crack length at the start of the crack propagation test Initial crack depth
A	Fatigue crack growth rate coefficient
A_{C1}	Temperature corresponding to the onset of austenisation during heating
A_{C3}	Temperature corresponding to the complete austenisation during heating
B	Thickness of the CT specimen
c_0	Initial crack half length
C	Normalised K-gradient
C_{eq}	Carbon equivalent
da/dn	Fatigue crack growth rate
K	Stress intensity factor
K_{max}	Maximum value of stress intensity factor
$K_{max,0}$	Maximum value of stress intensity factor at the start of the crack propagation test
K_{min}	Minimum value of stress intensity factor
$K_{min,0}$	Minimum value of stress intensity factor at the start of the crack propagation test
m	Fatigue crack growth rate exponent
n	Number of loading cycles
$N_{BS\,7910}$	Final number of loading cycles corresponding to the BS 7910 analysis
p	Fatigue crack growth rate parameter controlling the curvature in the near-threshold region
R	Load ratio
R_a	Average roughness
W	Width of the CT specimen

Greek symbols

ΔK	Stress intensity factor range
ΔK_0	Stress intensity factor range at the start of the crack propagation test
ΔK_{th}	Threshold stress intensity factor range
$\Delta K_{th,eff}$	Intrinsic component of the threshold stress intensity factor
$\Delta K_{th,lc}$	Threshold stress intensity factor range for long cracks
ΔP	Load range
$\Delta t_{8/5}$	Cooling time from 800 °C to 500 °C
$\Delta\sigma$	Stress range
σ_y	Yield strength

Acronyms

ACPD	Alternating current potential drop
BM	Base metal
CGHAZ	Coarse-grained heat-affected zone
CCT	Continuous cooling transformation
CT	Compact tension
FGHAZ	Fine-grained heat-affected zone
HAZ	Heat-affected zone
ICHAZ	Intercritical heat-affected zone
PD	Potential drop
TC	Thermocouple

studies have shown that even for long cracks, the microstructure can influence the crack growth rate [8–11]. Igwemezie et al. [12] investigated various structural steels, including S355, and attributed the observed differences in crack growth rates to the differences in observed crack-tip diversion, crack front bifurcation and metal crumb formation resulting from microstructural barriers.

Kim et al. [9] studied fatigue crack growth in the CGHAZ, fine-grained HAZ (FGHAZ) and base metal (BM) of the high-performance construction steel HSB800 and reported the highest crack growth rates in the CGHAZ, followed by the FGHAZ and the base metal. Similarly, the CGHAZ, FGHAZ and base metal of 18CrNiMo7-6 steel were studied in [8,10]. The CGHAZ exhibited higher crack growth rates than the FGHAZ. While these studies consistently indicate that the HAZ tends to show higher crack growth rates than the base metal, they do not include steels representative of those used in bridges constructed between the 1950s and 1980s. Notably, the base metals examined in [8–10] are of relatively high strength and hardness.

Several studies [13,14] have demonstrated that the varying hardness in the HAZ influences the crack growth rate of long cracks for which increasing hardness tends to decrease the crack growth rate. Fatigue cracks propagated from the base metal through the HAZ into the weld metal under constant ΔK and exhibited reduced crack growth rates when higher hardness was present ahead of the crack tip, even when the tip of the crack was not yet in the harder region. Furthermore, the presence of hard phases can act as local barriers to crack growth and may deflect the crack tip towards the more softer phase. Consequently, the resulting tortuous crack path increases the surface roughness and roughness-induced crack closure, reducing the crack growth rate [15].

Jayaprakash et al. [16] studied fatigue crack propagation in both the near-threshold region and Paris' regime for various hard-phase materials. They found that the pearlite phase exhibited the highest crack growth rate and lowest threshold stress intensity factor range ΔK_{th}, followed by bainite and martensite. In addition, larger grain sizes in the hard phases were associated with lower growth rates and higher ΔK_{th} values, corresponding to more frequent crack-tip deflections. These findings suggest that neglecting the influence of the HAZ microstructure on fatigue crack growth may lead to inaccurate predictions of fatigue crack propagation lives. Hardness, grain size, and grain morphology vary significantly across the HAZ. Moreover, for high-strength steels, in which the base metal may be harder than the HAZ, the reverse trend may occur, with the crack growth rate in the HAZ exceeding that in the base metal. This explain why, in [8–10], the base metal exhibited the lowest crack growth rates.

In this study, fatigue crack propagation tests were carried out on compact tension (CT) specimens exhibiting the distinct microstructures expected along the growth path of a crack in weldments in bridges constructed between the 1950s-1980s. These microstructures were simulated using a Gleeble thermal-mechanical simulator applied to the base metal of two different steels. The experimentally simulated microstructures were verified based on their phases, chemical composition, hardness and grain size. The experimental results from the fatigue crack propagation tests were used to estimate the remaining fatigue life of a weld toe crack in a T-joint and were compared to the analysis using only experimental results from the base metal and of the BS 7910 [17].

2. Materials and methods

2.1. Base metal

Three hypoeutectoid steels were considered in this study and these are hereafter referred to as Steels A, B and C. The experimental work

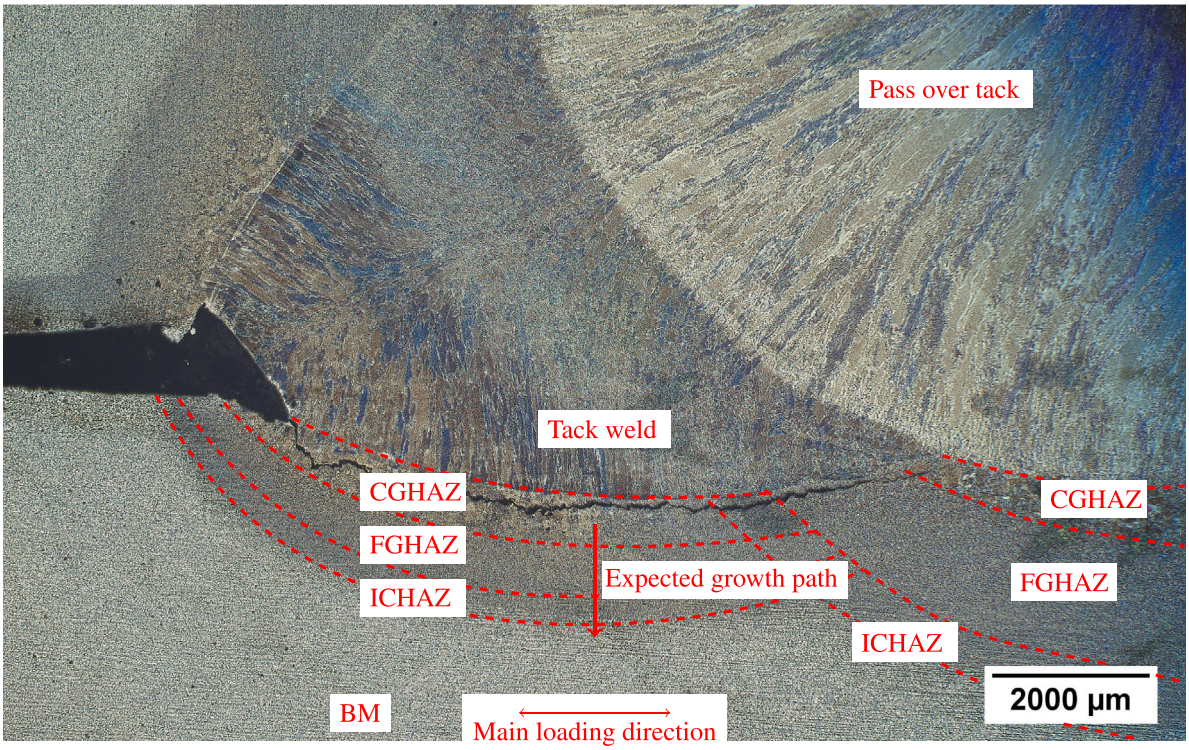


Fig. 1. Microscopic image of a sample of a weld taken from a bridge in the Netherlands containing a cold crack defect. The bridge was constructed in the 1980s and was made out of steel with a nominal yield stress of approximately 350 MPa. The defect was located in the weld of the main girder flange that had a thickness of 40 mm. The indicated regions are: CGHAZ = coarse-grained heat-affected zone, FGHAZ = fine-grained heat-affected zone, ICHAZ = intercritical heat-affected zone, and BM = base metal [6].

of the current study utilised Steels B and C and Steel A was used as reference. The chemical composition of all three Steels, determined through optical emission spectroscopy, are summarised in Table 2. The carbon equivalent, C_{eq}, was calculated according to [18]. The concentrations of Mo, V, Nb and Ti were each below 0.01 wt% while the concentration of B was less than 0.001 wt%. The main properties of the investigated steels are summarised in Table 1.

Steel A has a nominal yield strength of 350 MPa and originated from a bridge constructed in the 1980s, of which a welded connection is shown in Fig. 1, where a cold crack was identified in the flange of a main girder. Fig. 2(a) presents the microstructure of the base metal of Steel A. The average ferrite grain size and pearlite colony size are 14 µm and 9 µm, respectively, and an average hardness of 174 HV1 was measured.

Steel B was a newly manufactured steel of grade S355J2+N with a nominal yield strength of 355 MPa. Since no material could be extracted from Steel A for conducting fatigue crack growth experiments, Steel B was selected as a substitute due to its comparable carbon equivalent value. The microstructures of the different HAZ subregions and that of the base metal resulting from the experimental research have been compared to those observed in Steel A in a previous work [6]. Fig. 2(b) presents the microstructure of the base metal of Steel B. The average ferrite grain size and pearlite colony size are 13 µm and 11 µm, respectively, and an average hardness of 162 HV1 was measured.

Steel C, with a nominal yield strength of 235 MPa, was extracted from the web of a main girder of an old disassembled bridge constructed in 1950s. Fig. 2(c) presents the microstructure of the base metal of Steel C. The average ferrite grain size and pearlite colony size are 23 µm and 13 µm, respectively and an average hardness of 139 HV1 was measured.

Table 1
Main properties of the investigated steels.

	Nominal yield strength MPa	Vickers hardness HV1	Average ferrite grain size µm	Average pearlite colony size µm
Steel A	350	174	14	9
Steel B	355	162	13	11
Steel C	235	139	23	13

Table 2
Chemical composition and carbon equivalent of the investigated steels, given in wt%.

	C	Si	Mn	P	S	Cr	Cu	Ni	Al_{tot}	N	C_{eq}
Steel A	0.17	0.40	1.32	0.010	0.020	0.03	0.03	0.02	0.05	0.006	0.405
Steel B	0.15	0.19	1.40	0.015	0.009	0.05	0.03	0.02	0.03	0.003	0.397
Steel C	0.13	0.18	0.49	0.009	0.020	0.01	0.06	0.05	0.02	0.007	0.225

2.2. Experimental simulation of microstructures

Isolating the effects of a HAZ subregion of a welded specimen on crack propagation rates is difficult as these regions can be very thin (approximately 0.5 to 1.5 mm). In a previous work [6], these subregions were experimentally simulated using a Gleeble 3800 thermal-mechanical simulator. A short description of the experimental simulation is given in this section and a more detailed description is presented in [6].

The microstructures of the ICHAZ, FGHAZ and CGHAZ were experimentally simulated on coupon-shaped specimens. The base metal of Steels B and C (Section 2.1) were used in the experimental campaign. For each steel and each target HAZ subregion, three independent

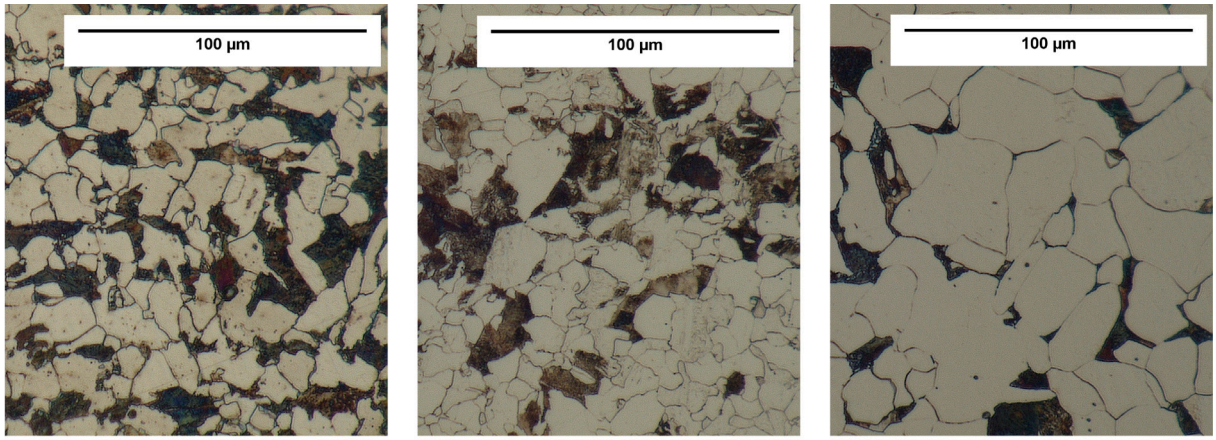


Fig. 2. Microstructures of the base metal of Steels: (a) A, (b) B and (c) C. Images were acquired at 1500× nominal magnification.

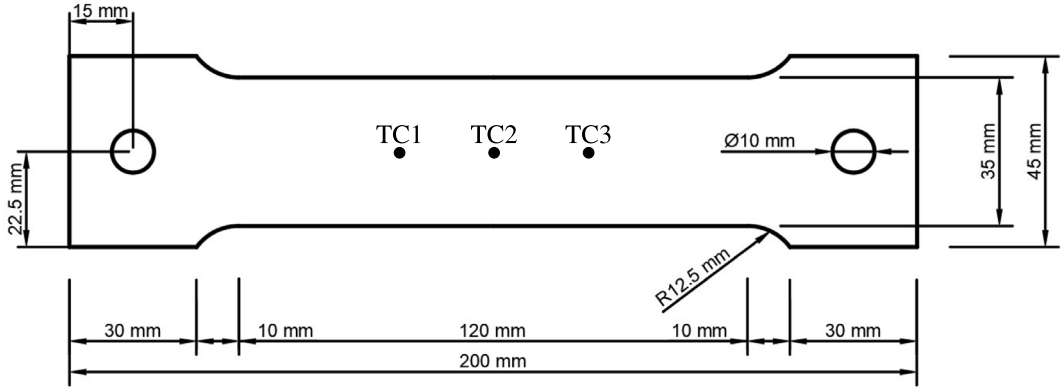


Fig. 3. Specimen used in the Gleeble experiment, created from base metal of Steels B and C, with dimensions in mm. The specimens had a thickness of 2 mm. The locations of the thermocouples (TC) are indicated with •.

coupon-shaped specimens were subjected to a single prescribed thermal cycle corresponding to either the ICHAZ, FGHAZ, or CGHAZ. Fig. 3 presents the dimension of the specimens used. The temperature–time curves were determined from a heat transfer analysis of the welding process of a fillet welded attachment (with a thickness of 10 mm) to a base plate (with a thickness of 40 mm) in Abaqus/CAE 2022 [19]. Fig. 4 shows the resulting temperature–time curves.

Fig. 5 presents the experimental set-up of the Gleeble simulations. The specimens were fixed to the copper grips in the Gleeble simulator using pins. A thermal load was applied to the specimens through conduction heating. All experimental simulations were executed in vacuum to avoid oxidation upon heating and the specimens were subsequently cooled with a combination of water and nitrogen gas. The traditional Gleeble setup uses a single nozzle to cool the specimen. This setup was modified to accommodate two cooling nozzles, thereby expanding the uniform cooling region. Additionally, mist nozzles were used to achieve a more homogeneous cooling of the specimen. Three thermocouples (TC) were spot-welded onto the specimen, spaced 25 mm apart. The middle thermocouple (TC2) provided feedback to the Gleeble, allowing the thermal load to be adjusted during the test. The two outer thermocouples (TC1 and TC3) confirmed that the thermal profile was uniform over the desired region. The maximum temperature differed at most 20 °C and the time above AC1 and AC3 differed at most 0.7 s. The thermocouple measurements are presented in [6]. Fig. 6 shows

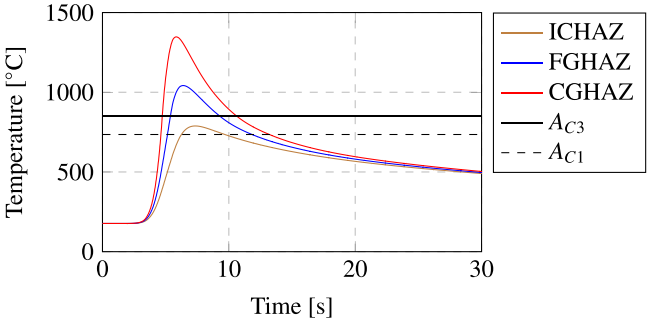


Fig. 4. Thermal cycles used for simulating HAZ microstructures.

that the experimentally simulated microstructure has a consistent microstructure over the entire fatigue crack. The tests were conducted load controlled and a relatively small load was maintained throughout the test (approximately 10 MPa) to ensure contact between the grips and the specimen. The specimens were free to deform upon heating and cooling to reduce the formation of residual stresses.

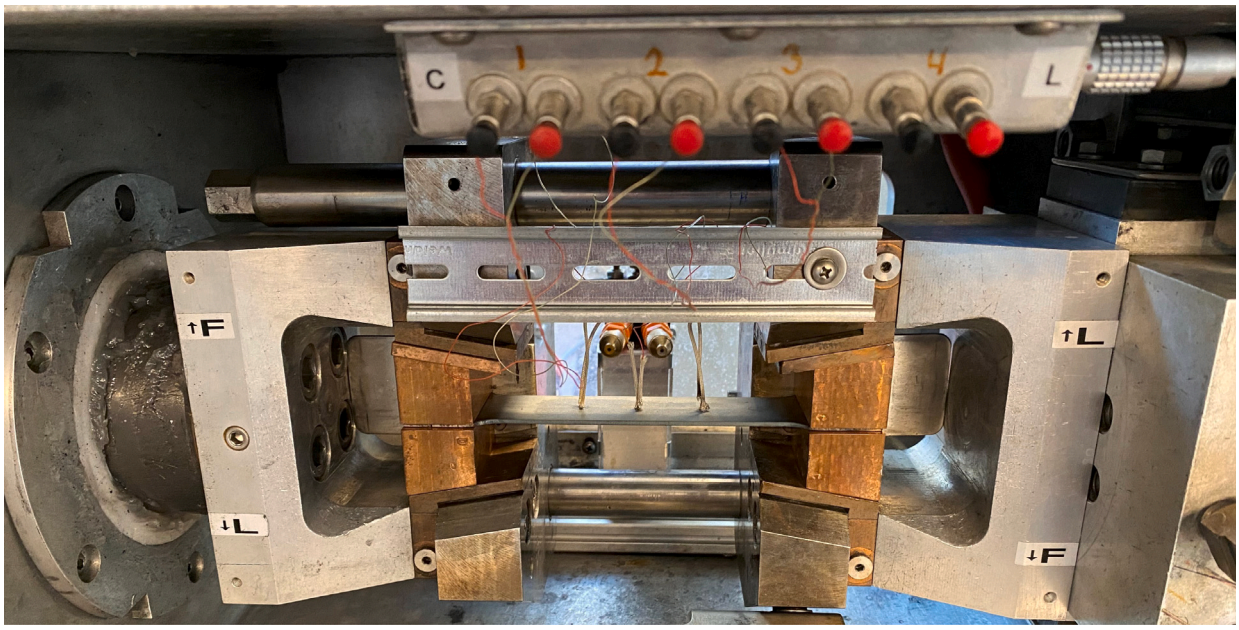


Fig. 5. Experimental set-up of the Gleeble.

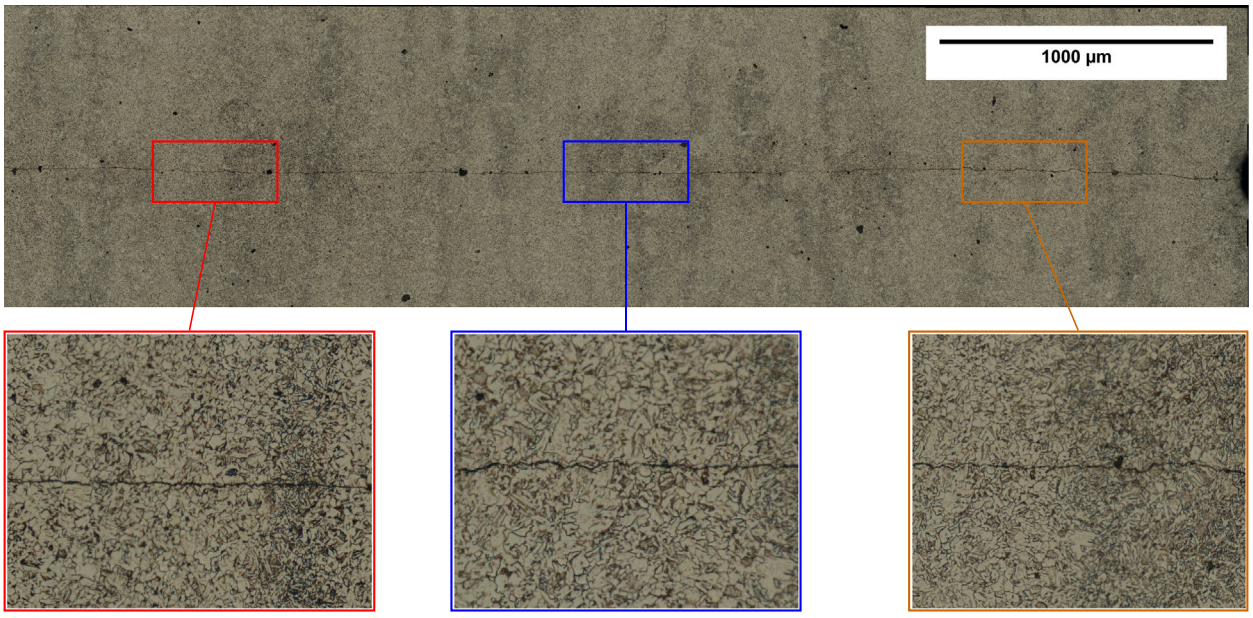


Fig. 6. Example of a crack in the experimentally simulated FGHAZ microstructure of Steel B. The lower images show enlarged views of the indicated regions.

Fig. 4 shows temperature–time curves used to experimentally simulate the microstructures of the HAZ subregions. The peak temperature of the ICHAZ was aimed in between the temperature corresponding to the onset of austenisation during heating (A_{C1}) and the temperature corresponding to the complete austenisation during heating (A_{C3}). The peak temperature of both the FGHAZ and the CGHAZ were aimed at 1020 °C and 1350 °C, respectively. Both were above A_{C3}, resulting in full austenisation upon heating. Values for A_{C1} and A_{C3} were determined based on the chemical compositions of the Steels [20]:

$$A_{C1} = 742 - 29 \cdot C - 14 \cdot Mn + 13 \cdot Si + 16 \cdot Cr - 17 \cdot Ni - 16 \cdot Mo + 45 \cdot V + 36 \cdot Cu \quad (1)$$

$$A_{C3} = 925 - 219 \cdot \sqrt{C} - 7 \cdot Mn + 39 \cdot Si - 16 \cdot Ni + 13 \cdot Mo + 97 \cdot V \quad (2)$$

The resulting A_{C1} and A_{C3} values were 722 °C and 838 °C for Steel B, and 735 °C and 849 °C for Steel C, for A_{C1} and A_{C3}, respectively.

Fig. 7 presents the microstructures resulting from the thermal-mechanical simulations conducted in the Gleeble. In the ICHAZ, the former pearlite colonies were austenised upon heating and transformed into refined pearlite and refined ferrite upon cooling. Former ferrite grains were not austenised upon heating. The entire microstructures of the FGHAZ and CGHAZ were austenised during the heating. Upon cooling, FGHAZ showed a refined ferrite/pearlite microstructure for

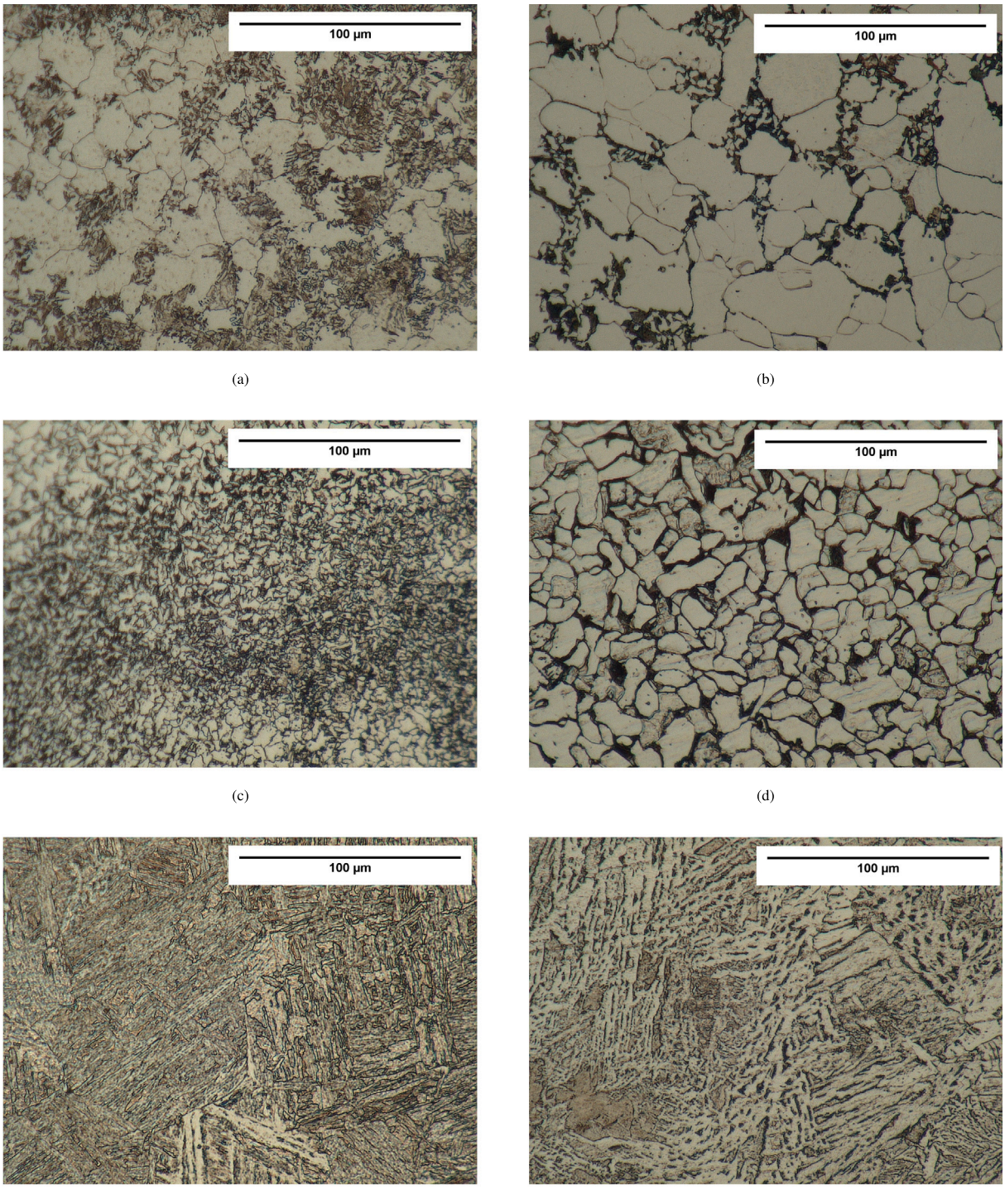


Fig. 7. Microscopic images for Steel B of the (a) ICHAZ, (c) FGHAZ and (e) CGHAZ; and for Steel C of the (b) ICHAZ, (d) FGHAZ and (f) CGHAZ, as experimentally simulated through the Gleeble 3800 apparatus. Images were acquired at 1500 × nominal magnification.

both Steels B and C. Figs. 8(a) and 8(b) show the continuous cooling transformation (CCT) diagrams for Steel B and C, respectively, together with the corresponding CGHAZ thermocouple measurements. The diagrams indicate that the CGHAZ of Steel B consists of a mixture of bainite and martensite, whereas the CGHAZ of Steel C consists predominantly of bainite.

2.3. Crack propagation tests

Compact tension (CT) specimens were extracted from the coupon-shaped specimens from Fig. 3, containing the experimentally simulated microstructures. Fig. 9(a) presents the location and orientation of the extracted CT specimens. Fig. 9(b) presents the dimensions of the CT specimen which was designed as per ASTM E647-23a [23].

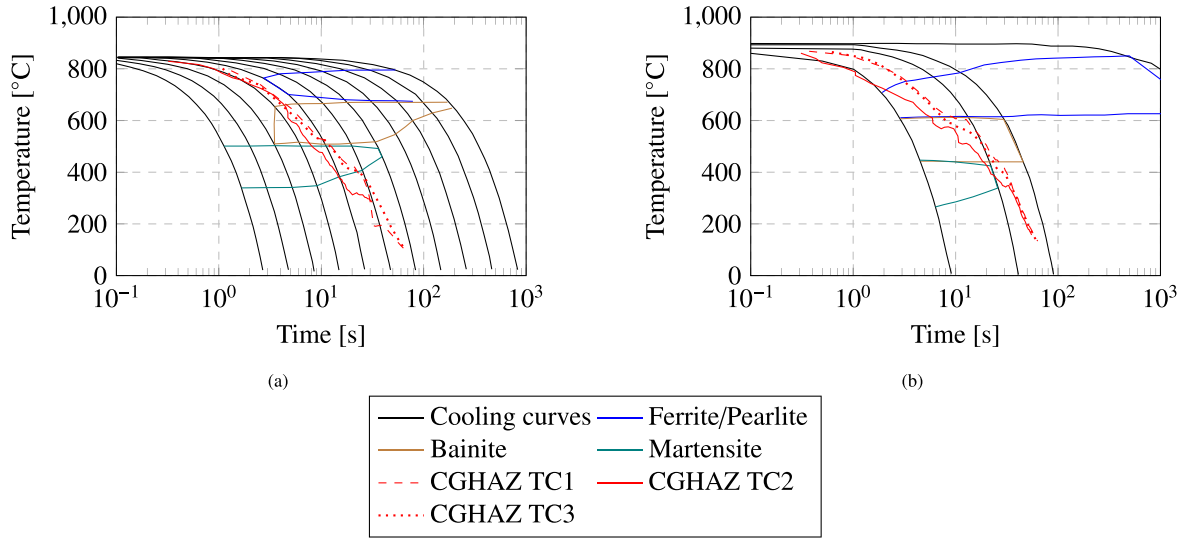


Fig. 8. CCT diagram with CGHAZ cooling curves at all three different thermocouples (TC) for indication of microstructure for (a) Steel B [21] and (b) Steel C [22].

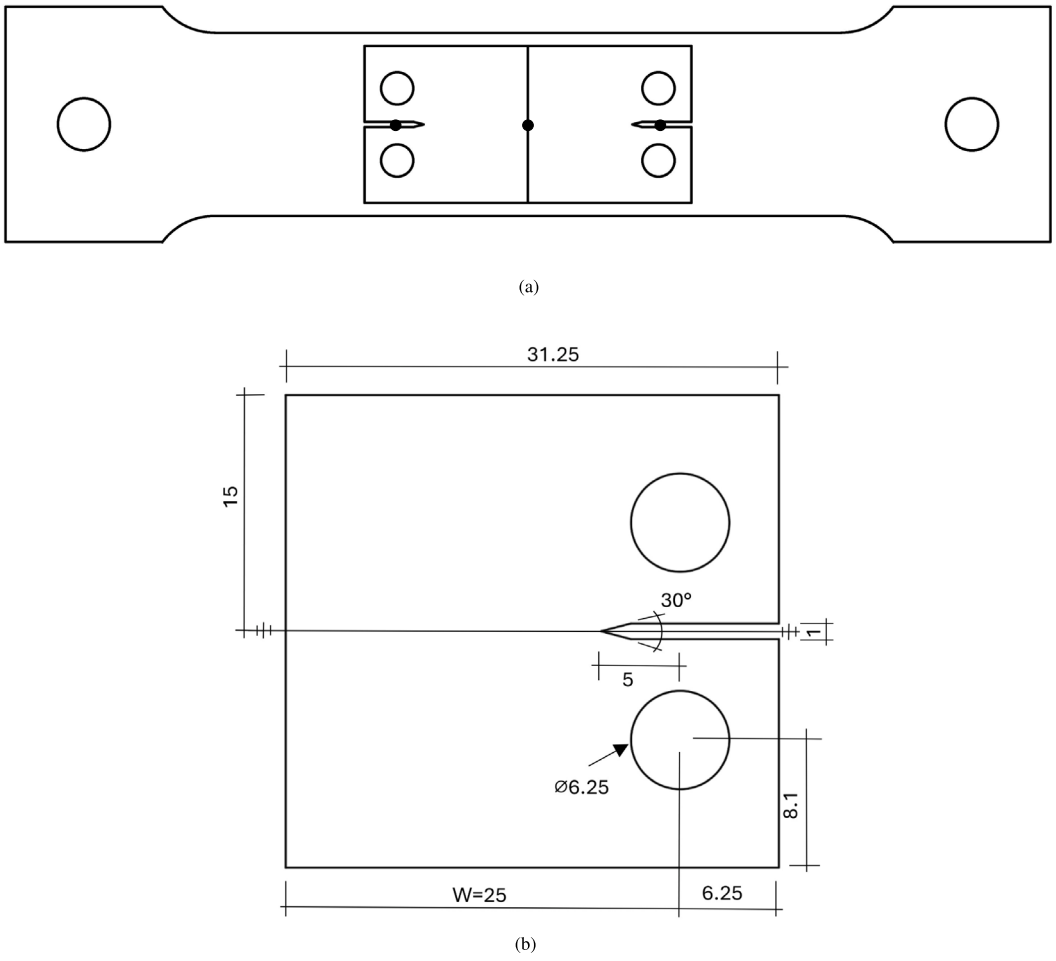


Fig. 9. Overview of the fatigue specimens with the (a) location of the extracted CT specimens within the coupon specimens and (b) the main dimensions of the CT specimens in mm. The thickness of both the coupon specimens and the CT specimens was 2 mm. The locations of the thermocouples are indicated with •.

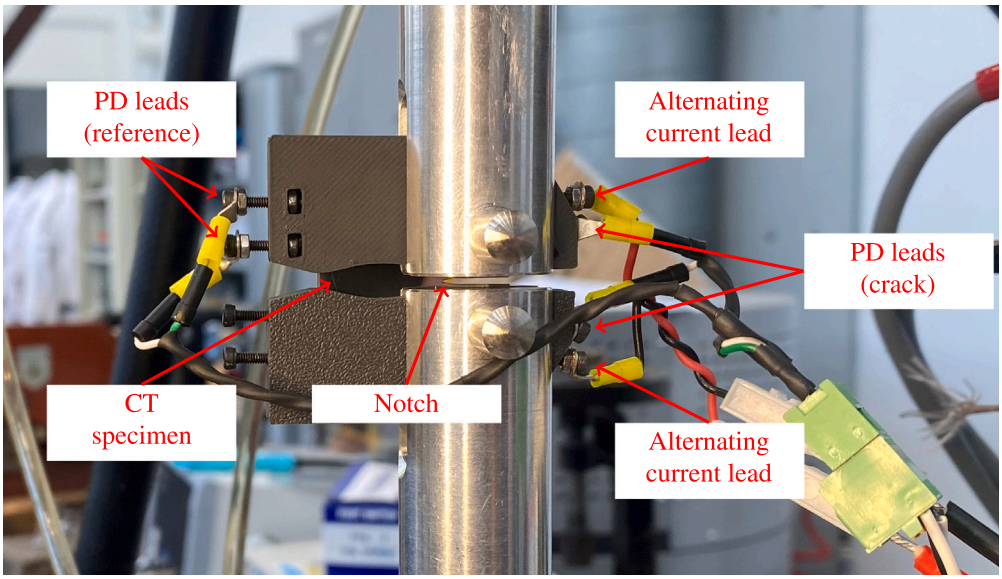


Fig. 10. Locations of ACPD leads used to measure the crack size throughout the tests (PD = potential drop).

Crack propagation tests were executed using a MTS Bionix tabletop test system. The tests were aimed at determining the near-threshold region (in-between the threshold stress intensity factor K_{th} and the Paris regime). The current study focuses on long cracks and the threshold stress intensity factor range determined in this study was that for long cracks ($\Delta K_{\mathrm{th,lc}}$). Short cracks may have lower threshold values [24] but are not part of this study. A sinusoidal load with a frequency of 60 Hz was used throughout the tests. Two different load ratios of $R = 0.1$ and $R = 0.5$ were applied in different tests. As the expected crack growth rates were relatively low, a ΔK-decreasing procedure was utilised as per ASTM E647-23a [23]. The normalised K-gradient, C, was used to define the load shedding selected as $C = -0.08\,\mathrm{mm}^{-1}$. This constant normalised K-gradient was used to define the curves for the minimum value of stress intensity factor, K_{min}, the maximum value of stress intensity factor, K_{max}, and the stress intensity factor range, ΔK, following [23] and utilised in the MTS system.

The minimum and maximum value of stress intensity at the start of the test were selected as $K_{\mathrm{min,0}} = 50\ \mathrm{MPa}\sqrt{\mathrm{mm}}$ and $K_{\mathrm{max,0}} = 500\ \mathrm{MPa}\sqrt{\mathrm{mm}}$, respectively, at the initial crack length a_0 for the tests at a load ratio of $R = 0.1$. For the tests at a load ratio of $R = 0.5$, the values were selected as $K_{\mathrm{min,0}} = 300\ \mathrm{MPa}\sqrt{\mathrm{mm}}$ and $K_{\mathrm{max,0}} = 600\ \mathrm{MPa}\sqrt{\mathrm{mm}}$.

The same load shedding procedure was used to create a pre-crack of 1 mm from the initial starter notch of 5 mm (see Fig. 9(b)) prior to the fatigue crack propagation test. The fatigue crack growth rates of the pre-cracking were not reported as these might be sensitive to notch effects [23]. The MTS system was programmed to accommodate the loading as per Eq. (4).

The stress intensity factor solution for CT specimens from ASTM E647-23a [23] has been used:

$$\Delta K = \frac{\Delta P}{B\sqrt{W}} \frac{(2+\alpha)}{(1-\alpha)^{3/2}} (0.886 + 4.64\alpha - 13.32\alpha^2 + 14.72\alpha^3 - 5.6\alpha^4) \quad (3)$$

where $\alpha = a/W$ for $a/W \geq 0.2$, ΔP is the load range, B is the thickness and W is the width of the specimen (as defined in Fig. 9(b)). Rewriting Eq. (3) leads to:

$$\Delta P = \Delta K \cdot B \cdot \sqrt{W} \cdot (1-\alpha)^{3/2} / ((2+\alpha) \cdot (0.886 + 4.64\alpha - 13.32\alpha^2 + 14.72\alpha^3 - 5.6\alpha^4)) \quad (4)$$

Throughout the test, the load was determined through Eq. (4). The crack length was measured in-situ and used as input to calculate the corresponding stress intensity factors.

Plane strain or plane stress conditions can be assumed according to the following criteria [25]:

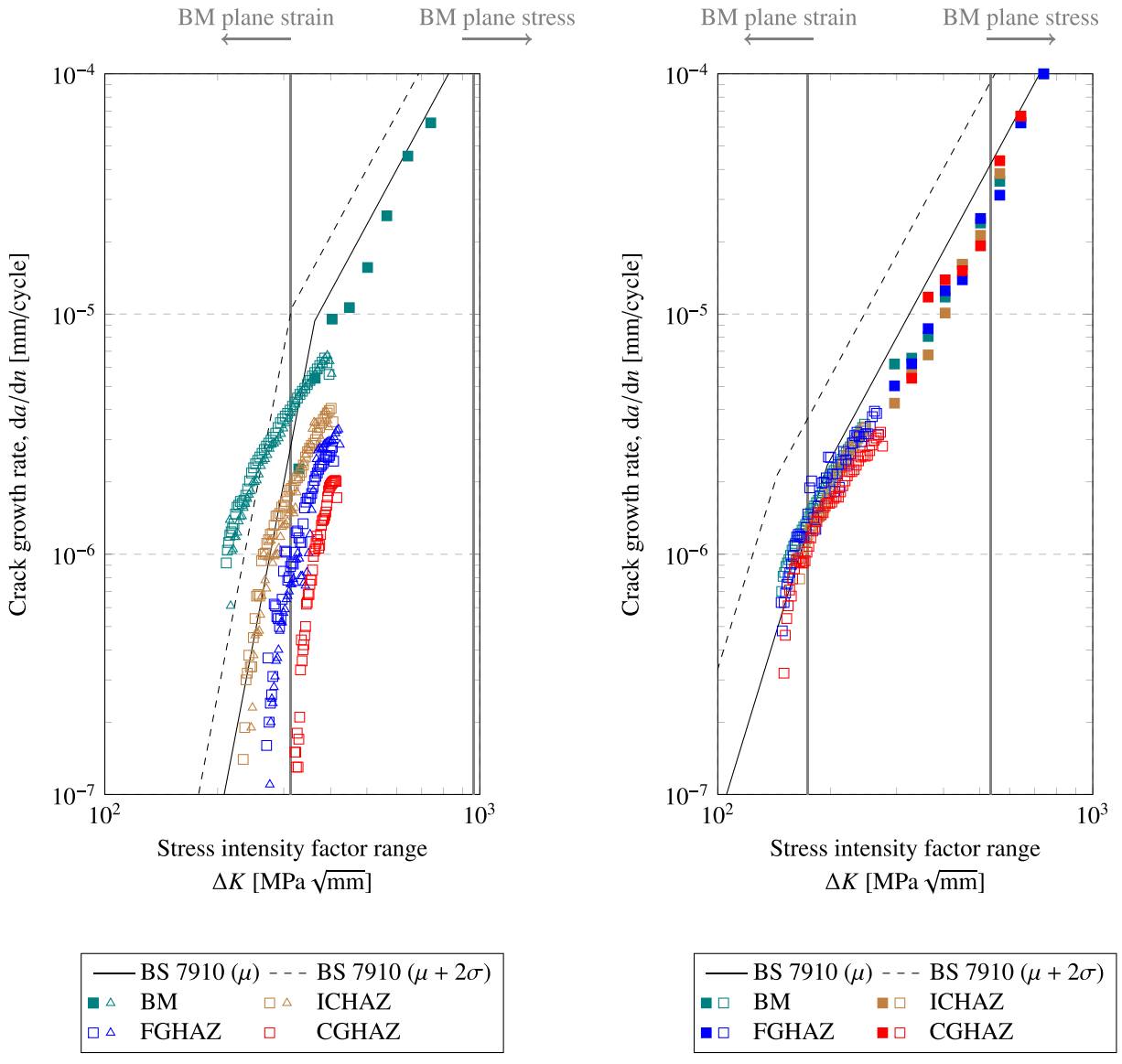
$$\begin{aligned} \Delta K &\leq \sigma_y (1-R)\sqrt{\frac{B}{3}} \quad \text{plane strain,} \\ \Delta K &\geq \sigma_y (1-R)\sqrt{\pi B} \quad \text{plane stress.} \end{aligned} \quad (5)$$

where σ_y is the yield strength. In between these criteria is the transition region where the conditions are neither full plane strain nor full plain stress. The nominal yield strength of Steel B and Steel C were 355 MPa and 235 MPa respectively (as presented in Table 1). The European SAFEBRICTILE project [26] yielded a ratio between the mean yield strength and the nominal yield stress of 1.25 and 1.2 for S235 and S355, respectively. Using these criteria and the mean yield strength, the majority of the test, is conducted in-between plane strain and plane stress conditions. Although the experimentally simulated HAZ subregions are expected to have higher yield strengths than their respective base metals, thereby favouring towards plane-strain conditions, their yield strengths were not measured.

To accommodate the computer-controlled load shedding, the crack was monitored using the alternating current potential drop (ACPD) method, utilising a Matelect CGM-7 apparatus [27]. A linear relationship between the potential drop over the crack and the crack length was derived separately for each individual subregion of Steels B and C through constant force amplitude (ΔK-increasing) tests [23] at a load ratio of $R = 0.5$ on CT-specimens with dimensions as presented in Fig. 9(b). One constant force amplitude test was performed at a load ratio of $R = 0.1$ for the base metal of Steel B. This confirmed that the linear relation was independent on the applied load ratio.

During the constant force amplitude tests, the crack lengths were measured optically while the potential drop was recorded using the Matelect CGM-7. The linear relationship varied among the studied microstructures as a result of differences in electrical resistivity. These individual linear relations for each microstructure were subsequently used to determine the crack length during the ΔK-decreasing tests.

Fig. 10 presents the ACPD set-up with the positions of the leads. The locations of the leads for the current and the potential drop measurement over the crack tip were selected as per ASTM E647-23a [23]. The specimen was too thin to screw the leads in the correct location. Alternatively, 3D printed casings were utilised to install the leads at



(a) Steel B, $R = 0.1$. (b) Steel B, $R = 0.5$.

Fig. 11. Experimental results of crack growth curves with the comparison to BS 7910 for Steel B at (a) $R = 0.1$ and (b) $R = 0.5$. Colours indicate the microstructural region. Filled and open symbols indicate ΔK-increasing and ΔK-decreasing tests, respectively. Different marker shapes indicate repetition tests.

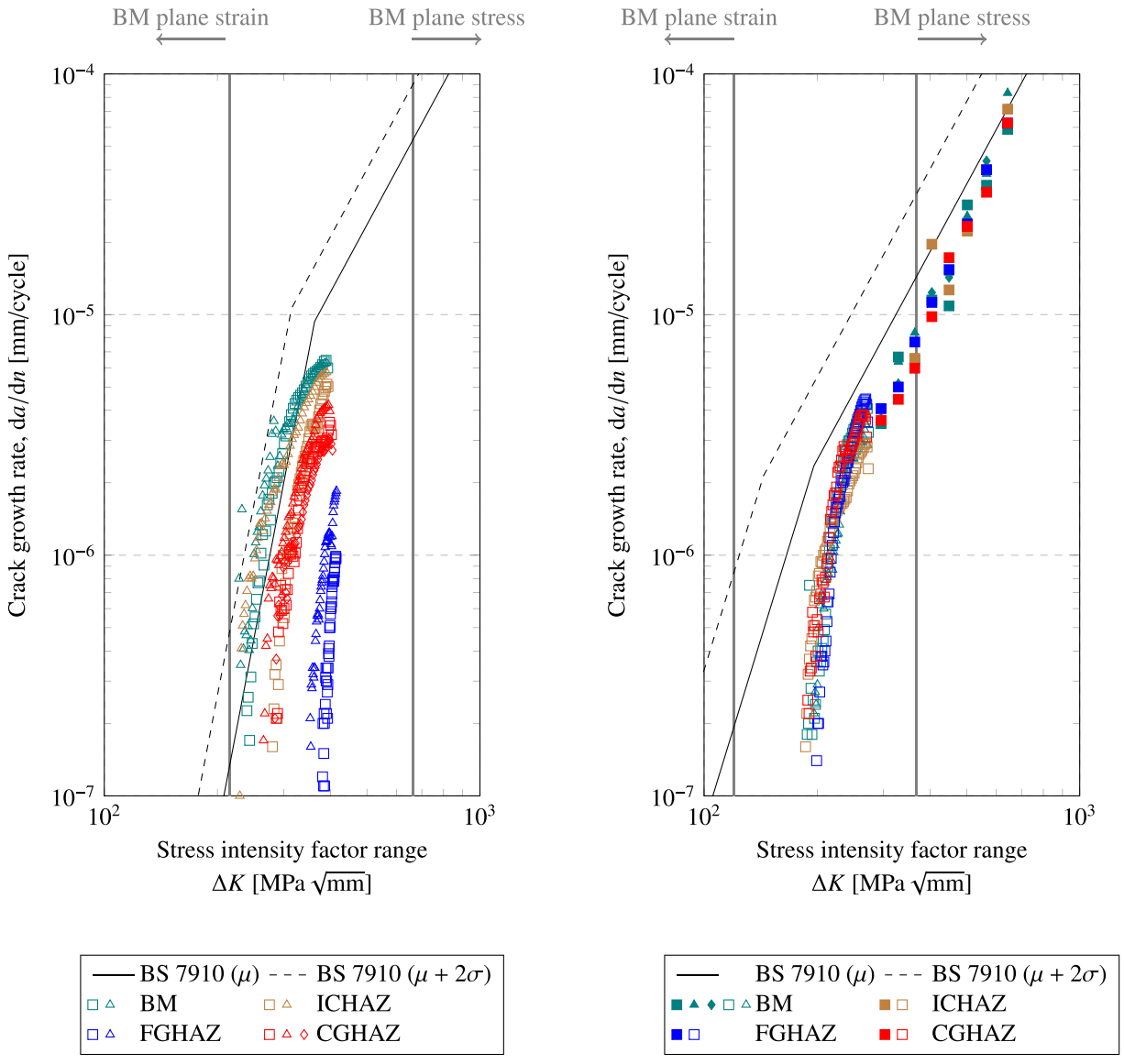
the correct location and to accommodate reproducibility throughout the experimental campaign.

An alternating current of 1 A at 5 kHz was used for the tests. The specimens were not electrically isolated from the MTS system as the impedance to the flow of current of the specimen is far lower than that of the parallel flow through the grips and loading apparatus [27]. The probability for a short circuit over the crack faces due to crack closure is negligibly small because of oxidation of the crack faces which significantly increases the electrical resistivity of the fractured surface [28,29].

3. Results

Figs. 11(a) and 11(b) present the results from the crack propagation tests of Steel B for $R = 0.1$ and $R = 0.5$, respectively. Different colours represent different microstructural regions and different symbols represent repetition tests for a region. Filled and open symbols indicate ΔK-increasing and ΔK-decreasing tests, respectively. The two-stage crack growth curves as well as the threshold stress intensity factor range ΔK_{th} provided by BS 7910 [17] are included as a comparison. The criteria for plane strain and plane stress, using base metal properties, were included as well. These suggest that the tests performed are neither in predominantly plane strain nor in predominantly plane stress conditions.

The results show that the crack growth rates observed at $R = 0.5$ do not differ significantly over the studied subregions. On the contrary, at $R = 0.1$, the differences in crack growth rate between the different subregions are much more pronounced. The base metal showed the highest crack growth rate followed by the ICHAZ, the FGHAZ and finally the CGHAZ. This trend holds over the entire domain of the studied ΔK values (between the threshold stress intensity factor for long cracks, $\Delta K_{\text{th,lc}}$, and 400 MPa$\sqrt{\text{mm}}$). The repetition tests showed consistent fatigue crack growth rates, giving confidence in the test procedure.



(a) Steel C, $R = 0.1$. (b) Steel C, $R = 0.5$.

Fig. 12. Experimental results of crack growth curves with the comparison to the BS 7910 for Steel C at (a) $R = 0.1$ and (b) $R = 0.5$ (b). Colours indicate the microstructural region. Filled and open symbols indicate ΔK-increasing and ΔK-decreasing tests, respectively. Different marker shapes indicate repetition tests.

Figs. 12(a) and 12(b) present the results from the crack propagation tests of Steel C for $R = 0.1$ and $R = 0.5$, respectively. As for Steel B, the crack growth rate was almost equal for the different subregions at $R = 0.5$, whereas a pronounced difference in crack growth rate between the subregions was observed at $R = 0.1$. The base metal showed the highest crack growth rates followed by the ICHAZ, the CGHAZ and finally the FGHAZ. This trend holds over the entire domain of the studied ΔK values (between $\Delta K_{\text{th,lc}}$ and 400 MPa$\sqrt{\text{mm}}$). Interestingly, the FGHAZ showed the lowest growth rate (and highest $\Delta K_{\text{th,lc}}$) which was not the case for Steel B.

Table 3 provides a summary of the results in which $\Delta K_{\text{th,lc}}$ and the fatigue crack growth rate coefficient, A, were determined from a least square method. Due to the finite specimen width, several tests ended before a crack growth rate of $\mathrm{d}a/\mathrm{d}n = 10^{-7}$ mm/cycle was reached. Consequently, $\Delta K_{\text{th,lc}}$ could not be determined consistently (i.e. for all tests) using the ASTM E647 [23] definition and hence, $\Delta K_{th,lc}$ was estimated using the fit of each test. The near threshold fatigue crack growth data were fitted using a reduced form of the Forman–Mettu relation [30]:

$$\mathrm{d}a/\mathrm{d}n = A \cdot \Delta K^m \cdot (1 - \Delta K_{\text{th,lc}}/\Delta K)^p \tag{6}$$

where m is the fatigue crack growth rate exponent and p is the parameter controlling the curvature in the near-threshold region. The least square fit was performed for the results in the near-threshold region for $\Delta K_{\text{th,lc}} \leq \Delta K \leq 400$ MPa$\sqrt{\text{mm}}$ and $\Delta K_{\text{th,lc}} \leq \Delta K \leq 300$ MPa$\sqrt{\text{mm}}$ for the results obtained at a load ratio of $R = 0.1$ and $R = 0.5$, respectively. Furthermore, as the results for $R = 0.5$ did not show significant difference between the various microstructures for each steel, the fit with the combined results was determined. The results for $R = 0.1$ with their corresponding fitted curves are presented in Appendix.

The experimental campaign was predominantly focussed on the near-threshold regime, with limited or no coverage of the Paris regime. Consequently, the fitted parameters cannot be used to extrapolate into the Paris regime.

Table 3
Overview of the fitting parameters from Eq. (6) obtained for Steels B and C for all subregions considered in the near-threshold region. The parameters are based on da/dN expressed in mm cycle^{-1} and $\Delta K_{th,lc}$ expressed in MPa$\sqrt{mm}$. Accordingly, A has units of mm cycle^{-1}/(MPa$\sqrt{mm}$)^m.

		R	A	m	p	$\Delta K_{th,lc}$
Steel B	BM	0.1	$1.3 \cdot 10^{-13}$	3.0	0.05	211
	ICHAZ	0.1	$1.0 \cdot 10^{-13}$	3.0	0.46	232
	FGHAZ	0.1	$9.3 \cdot 10^{-14}$	3.0	0.69	262
	CGHAZ	0.1	$1.2 \cdot 10^{-13}$	3.0	0.91	315
	BM+HAZ	0.5	$2.4 \cdot 10^{-13}$	3.0	0.02	165
Steel C	BM	0.1	$3.1 \cdot 10^{-13}$	3.0	1.01	209
	ICHAZ	0.1	$2.1 \cdot 10^{-13}$	3.0	0.63	253
	FGHAZ	0.1	$5.1 \cdot 10^{-13}$	3.0	1.58	355
	CGHAZ	0.1	$1.4 \cdot 10^{-13}$	3.0	0.87	265
	BM+HAZ	0.5	$8.3 \cdot 10^{-13}$	3.0	1.32	173

For all microstructures and load ratios examined in the current study, the crack propagated trans-granular as presented in Fig. 6 for the experimentally simulated microstructure of the FGHAZ of Steel B.

4. Discussion

The different microstructures in the current study had varying intrinsic parameters such as hardness, grain size and grain morphology that can influence the near threshold fatigue crack growth rate [31–33]. Harder phases may resist local plastic deformation and act as barriers to crack propagation. Depending on their distribution and morphology, they can deflect or branch the crack and produce interlocking of the fracture surfaces, thereby increasing $\Delta K_{th,lc}$ [31,33]. Conversely, a harder steel often has a higher yield strength which lowers the crack-tip plastic zone and may decrease plasticity-induced crack closure, lowering the $\Delta K_{th,lc}$ [34].

Grain size may similarly produce opposing effects. A finer microstructure contains more grain and phase boundaries per unit crack extension, which increases the total misalignment of slip planes with the principle stress, increasing $\Delta K_{th,lc}$ [15]. However, grain refinement often increases the yield strength of the material and thus reduces the plasticity induced closure. Hence grain refinement may also result in a reduction of $\Delta K_{th,lc}$ [34]. Finally, coarser grains may result in a higher roughness of the fatigue crack surface, which may increase roughness-induced closure and thus increase $\Delta K_{th,lc}$ [35].

In the present experimental campaign, environment, test frequency, specimen geometry, loading waveform and load-shedding procedure were held constant. The principal experimental variables were therefore the microstructure and load ratio. Comparison of the results at $R = 0.1$ and $R = 0.5$ provides an indication of whether the differences between the microstructures are predominantly associated with closure-sensitive mechanisms or with intrinsic crack-growth resistance. Similarly, the variations in hardness in this study enable evaluation of the net effect of hardness on the near-threshold crack growth rate.

At $R = 0.5$, no differences in fatigue crack growth rate were observed between the base metal and the simulated HAZ subregions of both steel grades, despite significant differences in hardness, grain size and phase composition. The overlap of the curves indicates that the intrinsic differences between the investigated microstructures did not influence the fatigue crack growth rate in the near-threshold region for this stress ratio, at which closure effects are expected to be less pronounced.

In contrast, pronounced differences in fatigue crack growth rates between the microstructures were observed at $R = 0.1$. For Steel B, the fatigue crack growth resistance increased in the order BM, ICHAZ, FGHAZ and CGHAZ. For Steel C, it increased in the order BM, ICHAZ, CGHAZ and FGHAZ. The fact that the differences became apparent at the lower load ratio suggests that crack closure mechanisms affected significantly the fatigue crack growth rate in the near threshold region at $R = 0.1$.

For Steel B, the measured hardness increased from 162 HV1 in the base metal to 168 HV1, 198 HV1 and 292 HV1 in the ICHAZ, FGHAZ and CGHAZ, respectively. At $R = 0.1$, the measured $\Delta K_{th,lc}$ increased in the same order (and the near-threshold fatigue crack growth rate decreased in this order), from 211 MPa$\sqrt{mm}$ to 232 MPa$\sqrt{mm}$, 262 MPa$\sqrt{mm}$ and 315 MPa$\sqrt{mm}$. Fig. 13(a) presents the hardness against the estimated value of $\Delta K_{th,lc}$.

The trend of Steel B of increasing $\Delta K_{th,lc}$ with increasing hardness is consistent with observations that hard constituents may restrict local plastic deformation and promote crack-tip deflection, crack-face interlocking and stress shielding [13,14,31–33]. The CGHAZ contained a bainitic/martensitic microstructure and had substantially greater hardness than the ferritic/pearlitic base metal and ICHAZ. Its lower growth rate at $R = 0.1$ compared to the other microstructures of Steel B may therefore result from a combination of greater local resistance and a more tortuous crack trajectory.

Nevertheless, hardness alone cannot be identified as the controlling parameter. If hardness had a direct effect on the intrinsic crack growth resistance, a similar trend would be expected at $R = 0.5$. The disappearance of the hardness-related trend at the higher load ratio instead suggests that the effect of hardness in Steel B was (at least partly) indirect, through changes in crack closure. The fact that $\Delta K_{th,lc}$ at $R = 0.1$ is higher than at $R = 0.5$ is in line with expectations based on crack closure, however, the fact that $\Delta K_{th,lc}$ at $R = 0.1$ increases instead of decreases with increasing hardness indicates that interlocking and similar effects described above are more important than plasticity-induced closure.

The results for Steel C do not show a similar trend between hardness and fatigue crack growth resistance as observed for Steel B. The hardness values of the BM, ICHAZ, FGHAZ and CGHAZ were 139 HV1, 133 HV1, 150 HV1 and 178 HV1, respectively, whereas the corresponding thresholds at $R = 0.1$ were 209 MPa$\sqrt{mm}$, 253 MPa$\sqrt{mm}$, 355 MPa$\sqrt{mm}$ and 265 MPa$\sqrt{mm}$. In particular, the FGHAZ exhibited the highest threshold and lowest crack growth rates, although it did not have the highest hardness. Furthermore, the ICHAZ was slightly softer than the base metal but exhibited a higher threshold. However, only a marginal difference in hardness is present between the different microstructures of Steel C. Hence, other microstructural features may dominate over the hardness-induced effects. Combining the results of both steel grades, the data are generally consistent, with one outlier that also contained the highest surface roughness.

A relevant difference between the microstructures of the FGHAZ and base metal of Steel C is the grain size. The ferrite grains and pearlite islands in the FGHAZ were approximately 10 μm and 5 μm, respectively, compared with approximately 23 μm and 13 μm in the base metal. Since crack propagation was transgranular in all specimens, the crack crossed more grain boundaries in the FGHAZ per unit length. For trans-granular fatigue crack growth, the crack propagates along slip planes whose orientation is determined by the local crystallography. The fact that the principal stress is not aligned with the slip planes results in a higher crack growth resistance [36].

In the Steel C specimens, the relatively high fatigue crack surface roughness of the FGHAZ and its high $\Delta K_{th,lc}$ are consistent with crack closure phenomena. The rougher surface might be a result of a harder second phase constituent in a softer matrix which enhanced the crack tip deflection. However, local hardness of different phases within a subregion were not measured.

Plasticity-induced crack closure originates from plastic deformation at the crack tip during cyclic loading. As the crack advances, plastically deformed material remains in the crack wake, which can cause premature contact between the crack faces during unloading [37,38]. Plasticity-induced crack closure is more pronounced in lower-strength material. The lower nominal yield strength of Steel C may have

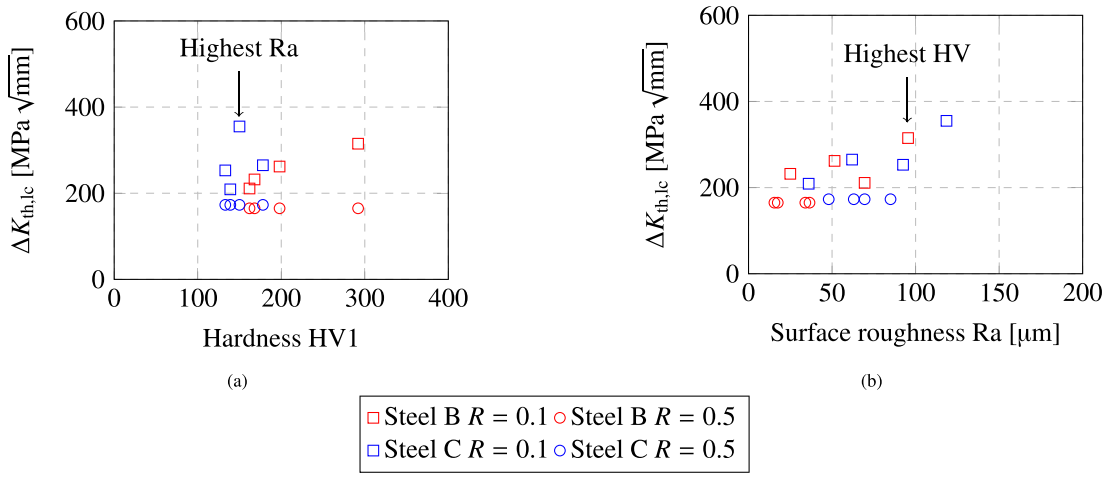


Fig. 13. Threshold stress intensity factor range for long cracks versus (a) hardness and (b) surface roughness.

contributed to differences between the two steels through plasticity-induced crack closure. The local yield strengths of the HAZ subregions could not be measured in the current study. However, a comparison should also consider differences in chemical composition, phase morphology and grain size.

Roughness-induced closure results from premature contact between mismatched crack surfaces and is enhanced by crack deflection, branching and mixed-mode loading [15,39]. Fig. 13(b) compares the measured average fracture-surface roughness of the fatigue crack faces with the corresponding $\Delta K_{th,lc}$. A general trend is observed between higher surface roughness and higher $\Delta K_{th,lc}$, particularly for Steel C. At $R = 0.5$, the threshold values remained unaffected regardless of variations in hardness and surface roughness.

Combining the aspects of the above discussion, it is expected that the differences in near-threshold fatigue crack growth resistance between the investigated microstructures at $R = 0.1$ were governed by roughness-induced crack closure. This is further supported by the clear correlation between surface roughness and $\Delta K_{th,lc}$. Differences in grain size, phase morphology, hardness and the presence of hard phases affect the local crack path. Increased crack-path tortuosity, crack-tip deflection and branching can increase the roughness of the crack faces, resulting into a higher degree of roughness-induced crack closure and consequently a lower effective stress intensity factor range and crack growth rate.

Since high tensile residual stresses are typically present in as-welded connections, the effective load ratio at the crack tip is relatively high [40] and crack closure effects exert a less dominant role compared to a case without residual stresses. Crack propagation behaviour in as-welded joints may therefore be represented by the data obtained at the stress ratio $R = 0.5$. However, in the case of significant relaxation of the welding-induced residual stress, crack closure effects occur, as represented by the crack propagation data obtained at $R = 0.1$, where crack closure effects are important, and the crack growth rate is influenced to a higher degree by the microstructure.

5. Fatigue crack growth of weld toe crack

To demonstrate the impact of the experimental findings of the current study, a fatigue crack growth analysis of a weld toe crack was performed using the experimental results of Steel B, as this is the more common steel used in bridges. The geometry of the T-joint shown in Fig. 1 was utilised, with a base plate thickness of 40 mm and a weld toe-to-weld toe distance of 26 mm. An illustration of the T-joint with the relevant geometric parameters is presented in Fig. 14. The three-dimensional stress intensity factor solution for a weld toe crack proposed by Bowness and Lee [41], as reported in BS 7910 [17], was used.

A weld toe crack with an initial aspect ratio of $a_0/c_0 = 0.5$ was chosen, where the initial crack depth, a_0, and the initial surface crack length, $2c_0$, were 0.15 mm and 0.6 mm, respectively, corresponding to approximate defect sizes observed in test specimens used for the S-N curves in the Eurocode [42]. Consequently, the early growth phase of the crack was treated as short crack growth. The model developed by Leonetti et al. [24] was used to account for short crack growth and the transition to long crack growth. In this model, the threshold stress intensity factor range and crack velocity function depend on the crack length and include the built up of extrinsic effects related to long cracks. The intrinsic component of the threshold stress intensity factor ($\Delta K_{th,eff}$) range was selected as 63 MPa$\sqrt{mm}$ [17].

A Python code was developed to perform the fatigue crack growth analysis. As the experimental campaign focussed on the near-threshold region, the growth analysis was terminated when the stress intensity factor range exceeded the domain covered by the experimental data.

A stress range with an external load ratio of 0.1 was applied to the base plate as presented in Fig. 14. Four stress ranges, $\Delta\sigma$, were considered, namely, 125 MPa, 150 MPa, 175 MPa and 200 MPa. These stress ranges are common in bridge application and were therefore selected.

Two cases were studied. Firstly, an as-welded condition was represented by a constant effective load ratio of $R = 0.5$, by considering the crack growth rate parameters obtained for $R = 0.5$. In [40] it was demonstrated that, for the growth of a weld toe crack in the actual residual stress field, the effective stress intensity factor ratio remained approximately constant and close to a value of 0.5. Secondly, the theoretical case of full relaxation of residual stress was taken into account by considering the crack growth rate parameters obtained for $R = 0.1$. Subsequently, for both cases, fatigue crack growth analysis was carried out for the following three scenarios:

1. Crack growth curve according to the mean two-stage curve of the BS 7910 [17] (as presented in Figs. 11 and 12, in which a distinction between microstructures is not included).
2. Crack growth curve based on the experimental fit for the base metal of Steel B, as presented in Table 3.
3. Crack growth curves considering the heterogeneous microstructure by including the individual subregions in the prediction

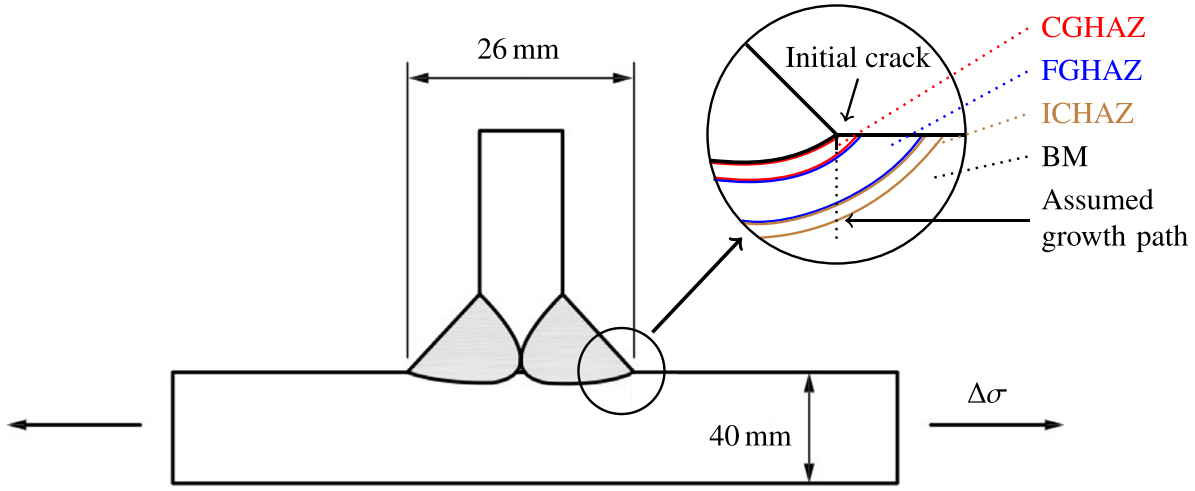


Fig. 14. Weld toe crack of a T-joint with a membrane stress applied to the base plate in transverse direction. The various subregions in the HAZ are indicated with the various colours. The initial crack is located at the weld toe and the assumed crack path is through the base plate.

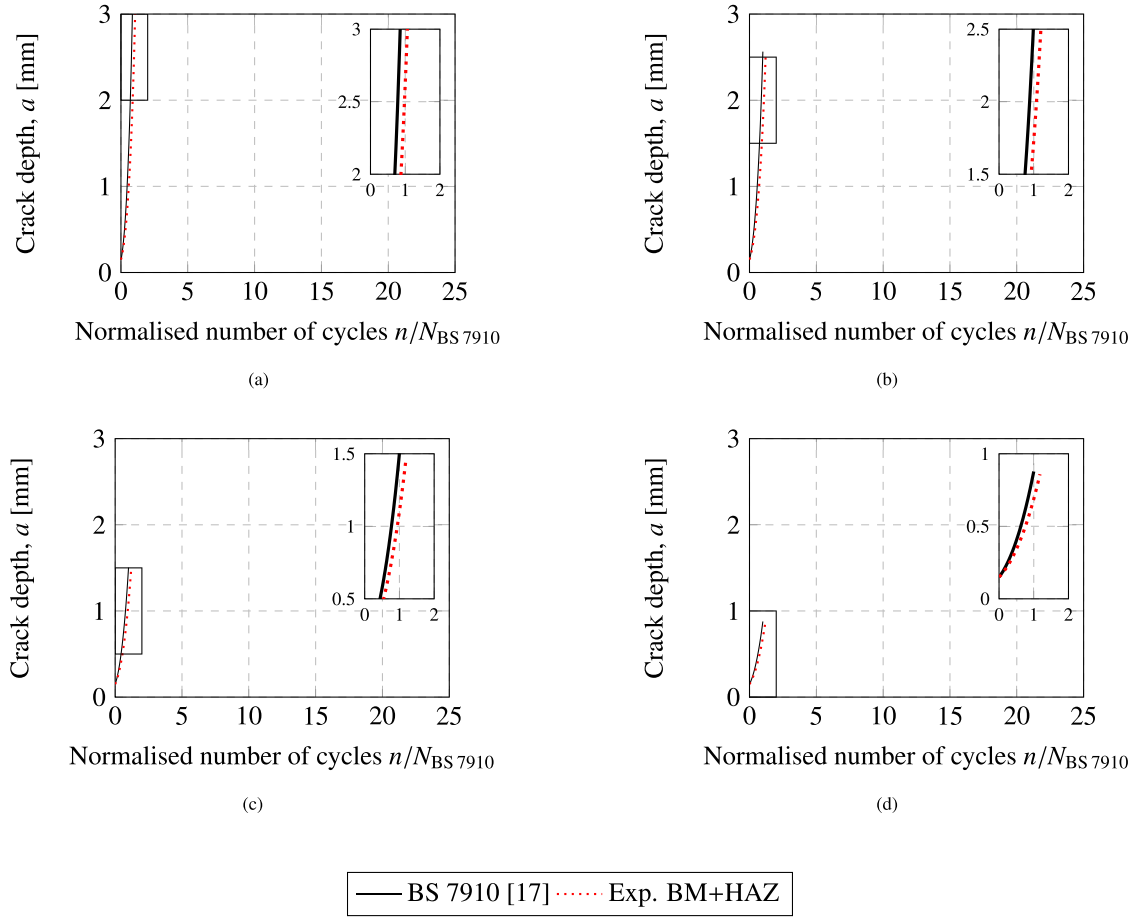


Fig. 15. Comparison of crack growth results in the as-welded joint at a stress range of (a) $\Delta\sigma$ = 125 MPa, (b) $\Delta\sigma$ = 150 MPa, (c) $\Delta\sigma$ = 175 MPa and (d) $\Delta\sigma$ = 200 MPa.

model based on the experimental fits for the base metal and the different HAZ subregions of Steel B, as presented in Table 3 (this results in the combined fit for the as-welded case).

The widths of the HAZ subregions were measured from the sample presented in Fig. 1. These resulted into 0.6 mm, 1.7 mm and 0.5 mm for the CGHAZ, FGHAZ and ICHAZ, respectively. Crack growth curves from

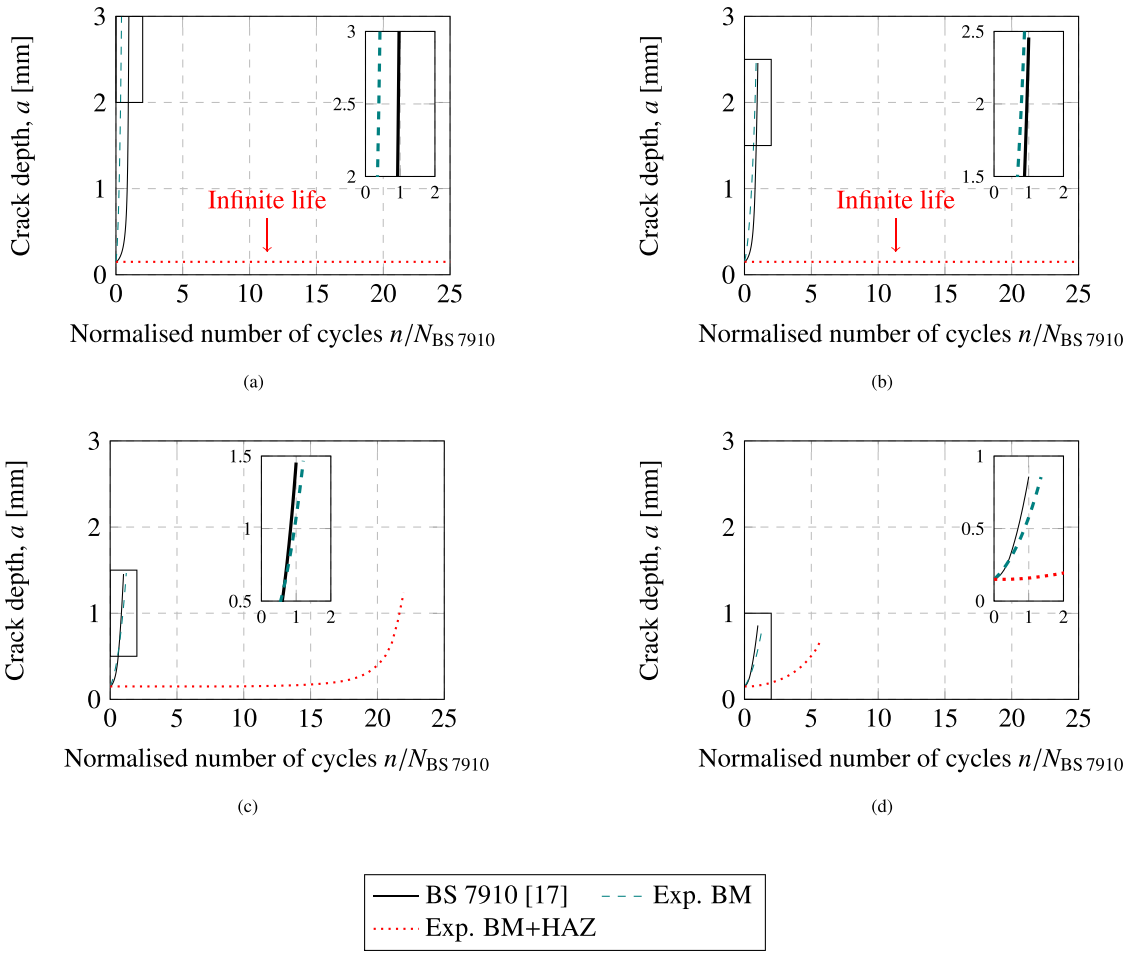


Fig. 16. Comparison of crack growth results in the theoretical case of full relaxation of residual stress at a stress range of (a) $\Delta\sigma = 125$ MPa, (b) $\Delta\sigma = 150$ MPa, (c) $\Delta\sigma = 175$ MPa and (d) $\Delta\sigma = 200$ MPa.

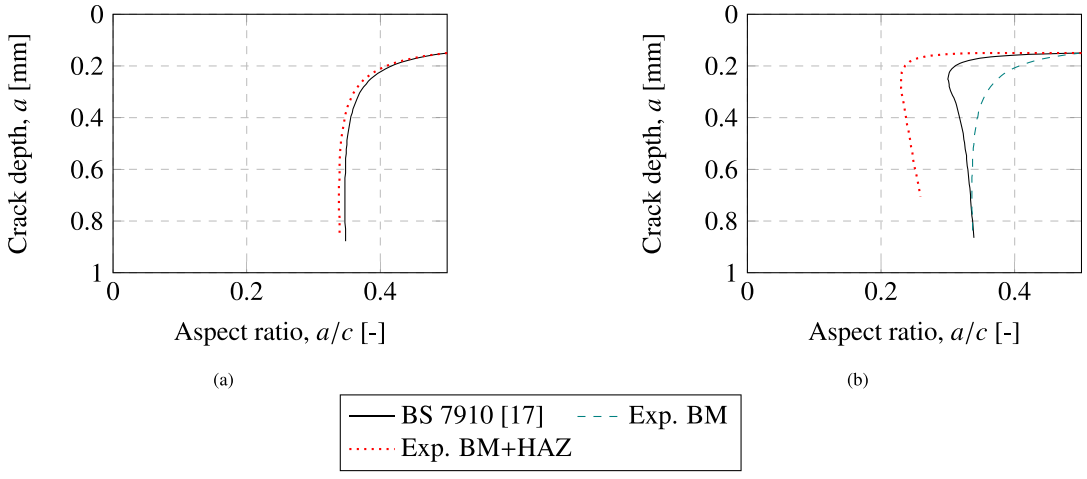


Fig. 17. Crack aspect ratio as a function of crack depth for the (a) as-welded joint and (b) the theoretical case of full relaxation of residual stress.

the experimental fit presented in Table 3 were applied according to the location of the tip of the crack (only for Scenario 3).

Fig. 15 presents the results of the fatigue crack growth analysis in the as-welded connection (using the experimental results for Steel B at $R = 0.5$) and Fig. 16 presents the results of the theoretical case of full relaxation of the welding-induced residual stress (using the experimental results for Steel B at $R = 0.1$). The resulting number of cycles, n, were normalised by the final number of cycles corresponding to the

analysis using the crack growth curves according to BS 7910 [17], $N_{\mathrm{BS\,7910}}$ (Scenario 1).

The results show that, in the as-welded case (Fig. 15), the results incorporating the crack growth rates from the experimental study (resulting final values for normalised number of cycles of 1.23, 1.21, 1.19 and 1.18 for stress ranges of 125 MPa, 150 MPa, 175 MPa and 200 MPa, respectively) are close to the results when considering the BS 7910 [17] (with final values for normalised number of cycles of 1.0). However, in the theoretical case of full relaxation of residual stresses (Fig. 16), there is a large difference between the normalised number of cycles when considering the heterogeneous microstructure of the HAZ as compared to the base metal and the BS 7910 [17]. The fatigue life was approximately 6 and 22 times longer as compared to the estimation by the BS 7910 at a stress range of 200 MPa and 175 MPa, respectively. This is due to the relatively small crack growth rates observed in the CGHAZ of Steel B as compared to the BS 7910 curves, as presented in Fig. 11. The fatigue life was infinite at a stress range of both 100 MPa and 125 MPa when considering the HAZ as the stress intensity factor ranges remained below ΔK_{th}.

Previous studies [43,44] showed that for a given geometry and loading condition the aspect ratio of a fatigue crack converges asymptotically depending on the boundary conditions and cross section geometry. However, these studies considered materials characterised by a uniform microstructure. Fig. 17 presents for Steel B the crack aspect ratio a/c against the crack depth a for the as-welded joint (Fig. 17(a), using $R = 0.5$) and the case of full relaxation of the residual stresses (Fig. 17(b), using $R = 0.1$). For the as-welded joint, the crack aspect ratio of the results utilising the experimental findings closely match those of the BS 7910 [17] and converge from the initial aspect ratio of $a_0/c_0 = 0.5$ to a value of approximately $a/c = 0.35$. In the theoretical case of full relaxation of the welding-induced residual stress, the aspect ratios when considering experimental fit of the base metal and the BS 7910 converge to a value of $a/c = 0.35$ (which is in agreement with [45]), similar as in the case of the as-welded joint. Considering the heterogeneous microstructure of the HAZ, the aspect ratio was significantly lower and did not reach a stable value before the end of the simulation.

For the crack growth prediction models using a uniform microstructure, the crack aspect ratio converges to a value of $a/c = 0.35$. However, in the case of full relaxation, the heterogeneous HAZ microstructure of the studied Steel B lowers the crack aspect ratio.

The results obtained using the BS 7910 bi-linear curve and those considering the heterogeneous HAZ microstructure both show an initial steep decrease in aspect ratio, followed by a small increase. This behaviour is caused by the different stress intensity factor ranges at the surface than in depth of the semi-elliptical crack front, combined with the non-linear shape of the applied crack growth curves. Initially, the stress intensity factor range at the surface point is larger than in depth. In the analysis considering the heterogeneous microstructure of the HAZ, the deepest point is initially below the ΔK_{th} of the CGHAZ, whereas the surface point is above. In the BS 7910 analysis, the deepest point is initially located on the lower branch of the bi-linear crack growth curve, while the surface point is located on the upper branch. Consequently, the crack initially grows faster along the surface then in depth direction, causing the aspect ratio a/c to decrease.

As the crack length increases, the stress intensity factor range at the deepest point also increases. Once the stress intensity factor at the deepest point of the crack exceeds the ΔK_{th} of the CGHAZ (in the case considering heterogeneous microstructure of the HAZ) or reaches the transition to the upper branch of the BS 7910 curve (in the case considering the BS 7910 bi-linear curve), growth in depth direction accelerates and the aspect ratio a/c increases again. As the initial stress intensity factors of both the surface and deepest point were above ΔK_{th} of the base metal of Steel B, this initial decrease and subsequent increase of the aspect ratio a/c was not observed.

6. Concluding remarks

Fatigue crack growth tests were conducted to obtain crack propagation data in the near-threshold region using a ΔK-decreasing test procedure. The base metals used in the experimental campaign had nominal yield strength of 355 MPa (Steel B) and 235 MPa (Steel C). The HAZ subregions were experimentally simulated using the corresponding base metals. Two load ratios, $R = 0.1$ and $R = 0.5$, were applied. Crack growth was monitored using an ACPD set-up, which was calibrated for each base metal and HAZ subregion separately. The main conclusions are as follows:

- At $R = 0.5$, no significant difference was observed between the simulated HAZ subregions and their respective base metals because crack closure effects are largely suppressed.
- For both steels, the experimentally simulated HAZ subregions showed lower crack growth rates and higher $\Delta K_{\mathrm{th,lc}}$ than their respective base metals at $R = 0.1$. This behaviour is attributed to increased roughness-induced crack-closure in the near-threshold region. For Steel B, the crack growth rates decreased with increasing hardness and surface roughness. For Steel C, where the hardness differences between the studied microstructures were smaller, the lower crack growth rates of the experimentally simulated HAZ subregions compared to the base metal, were mainly attributed to roughness induced crack-closure due to an increase in fatigue crack surface roughness.
- For as-welded joints with high constraint, where cracks propagate under high load ratio as a result of welding-induced residual stresses, there is no appreciable influence of the microstructure on the fatigue crack growth. However, in the case of relaxation of the welding-induced residual stress, there is a significant influence of the microstructure on the fatigue crack growth rate.
- For Steel B, accounting for the heterogeneous HAZ microstructure resulted in predicted fatigue lives that were approximately 22 and 6 times longer than those obtained using BS 7910 at stress ranges of 175 MPa and 200 MPa, respectively.

CRediT authorship contribution statement

David Malschaert: Writing – original draft. **Anis Mohabeddine:** Writing – review & editing, Supervision. **Milan Veljkovic:** Writing – review & editing, Writing – original draft, Supervision. **Davide Leonetti:** Writing – review & editing. **Johan Maljaars:** Writing – review & editing, Writing – original draft, Supervision.

Declaration of competing interest

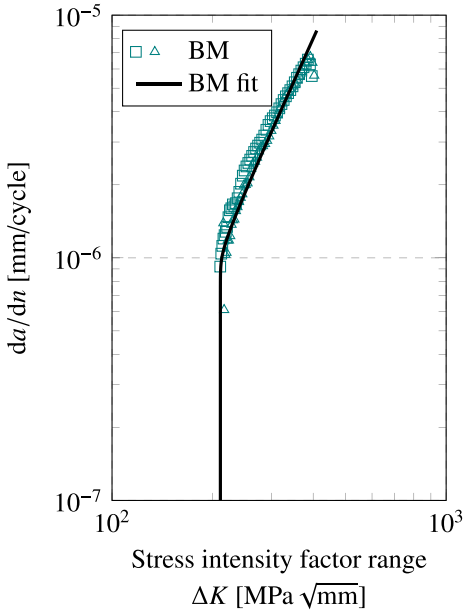
The authors declare that they have no known competing financial interests or personal relationships that could have appeared to influence the work reported in this paper.

Acknowledgements

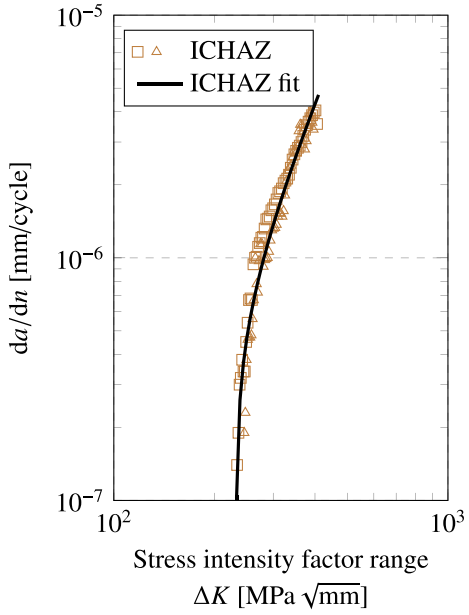
This research was carried out under project number T20006c in the framework of the Research Program of the Materials innovation institute (M2i) (www.m2i.nl) supported by Rijkswaterstaat and ProRail. The first author would like to thank Raymond Dekker, Elise Reinton and Ton Riemslag for the assistance with the experimental set-up that benefited this research.

Appendix. Fatigue crack growth curves

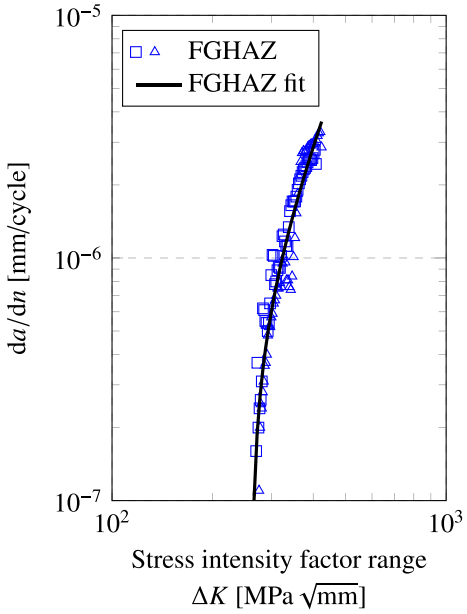
Figs. A.18 and A.19 present the near-threshold fatigue crack rate results of each individual microstructure studied at a load ratio of $R = 0.1$ for Steel B and Steel C, respectively. The graphs include the fit using the parameters presented in Table 3 and Eq. (6).



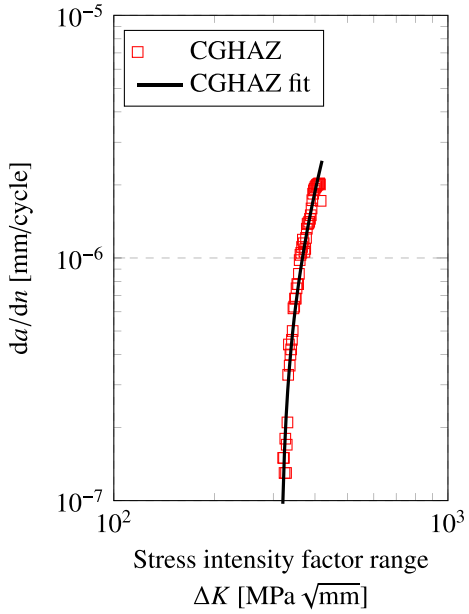
(a) BM of Steel B, $R = 0.1$.



(b) ICHAZ of Steel B, $R = 0.1$.

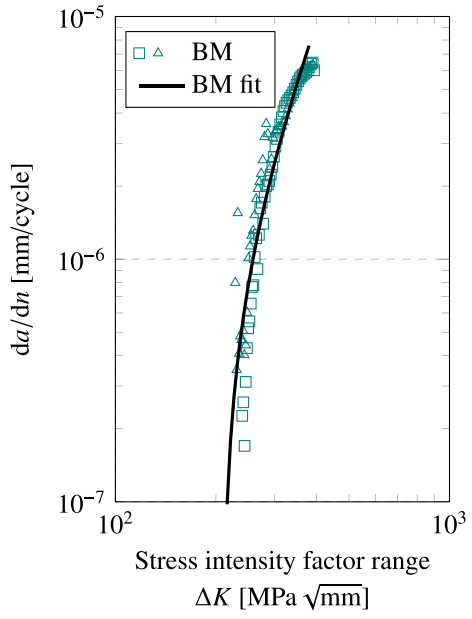


(c) FGHAZ of Steel B, $R = 0.1$.

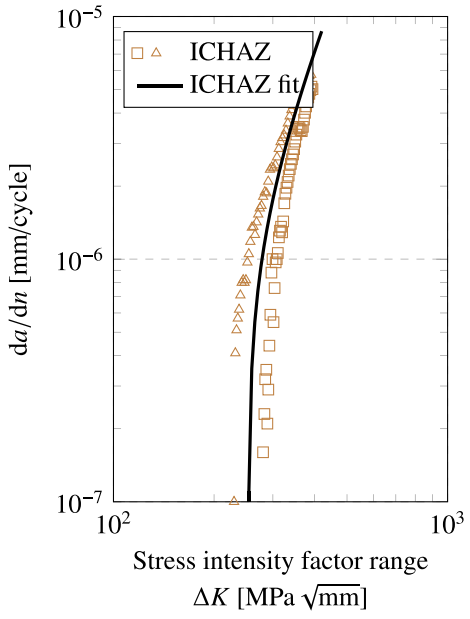


(d) CGHAZ of Steel B, $R = 0.1$.

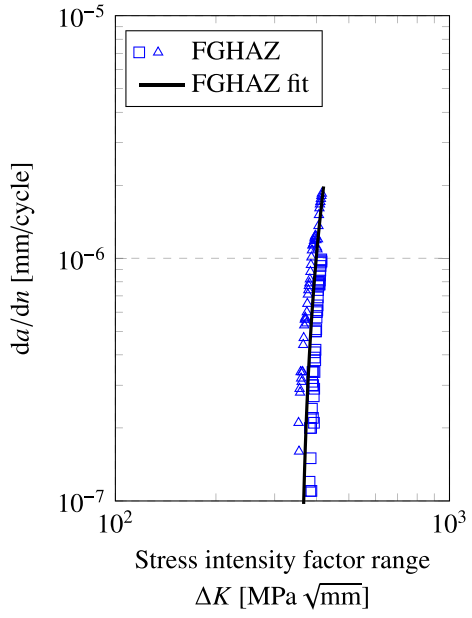
Fig. A.18. Near-threshold fatigue crack growth results for Steel B at $R = 0.1$ including the fit according to Table 3 and Eq. (6) for (a) BM, (b) ICHAZ, (c) FGHAZ and (d) CGHAZ.



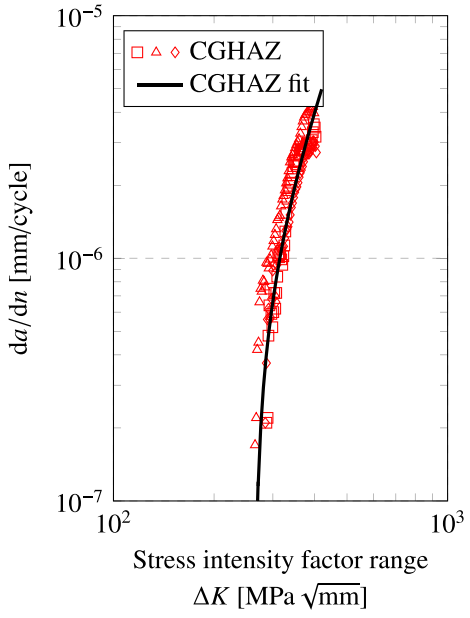
(a) BM of Steel c, $R = 0.1$.



(b) ICHAZ of Steel c, $R = 0.1$.



(c) FGHAZ of Steel c, $R = 0.1$.



(d) CGHAZ of Steel c, $R = 0.1$.

Fig. A.19. Near-threshold fatigue crack growth results for Steel C at $R = 0.1$ including the fit according to Table 3 and Eq. (6) for (a) BM, (b) ICHAZ, (c) FGHAZ and (d) CGHAZ.

Data availability

Data will be made available on request.

References

[1] Kolstein MH. Fatigue classification of welded joints in orthotropic steel bridge decks. Delft University of Technology; 2007.

[2] Kühn B, Lukic M, Nussbaumer A, Günther H-P, Helmerich R, Herion S, Kolstein MH, Walbridge S, Androic B, Dijkstra O, et al. Assessment of existing steel structures: recommendations for estimation of remaining fatigue life. Joint Research Center; 2008.

[3] Lesiuk G, Correia JA, Krechkovska HV, Pekalski G, de Jesus AM, Student O. Degradation theory of long term operated materials and structures. Springer; 2021.

[4] Kvackaj T, Bidulská J, Bidulskỳ R. Overview of HSS steel grades development and study of reheating condition effects on austenite grain size changes. Materials 2021;14(8):1988.

[5] Zerbst U. Application of fracture mechanics to welds with crack origin at the weld toe: A review part 1: Consequences of inhomogeneous microstructure for materials testing and failure assessment. Weld World 2019;63(6):1715–32. http://dx.doi.org/10.1007/s40194-019-00801-5.

[6] Malschaert D, Mohabeddine A, Veljkovic M, Leonetti D, Maljaars J. Microstructures of the heat-affected zone around a cold crack in weldments. J Constr Steel Res 2026. http://dx.doi.org/10.1016/j.jcsr.2026.110436.

[7] Kucharczyk P, Madia M, Zerbst U, Schork B, Gerwien P, Münstermann S. Fracture-mechanics based prediction of the fatigue strength of weldments. Material aspects. Eng Fract Mech 2018;198:79–102. http://dx.doi.org/10.1016/j.engfracmech.2017.09.010.

[8] Vuherer T, Smaili F, Bjelajac E, Manjgo M, Lojen G. Simulation and mechanical properties of fine-grained heat-affected zone microstructure in 18CrNiMo7-6 steel. Mater 2022;15(19):6782. http://dx.doi.org/10.3390/ma15196782.

[9] Kim S, Kang D, Kim T-W, Lee J, Lee C. Fatigue crack growth behavior of the simulated HAZ of 800 MPa grade high-performance steel. Mater Sci Eng A 2011;528(6):2331–8. http://dx.doi.org/10.1016/j.msea.2010.11.089.
[10] Smaili F, Lojen G, Vuherer T. Fatigue crack initiation and propagation of different heat affected zones in the presence of a microdefect. Int J Fatigue 2019;128:105191. http://dx.doi.org/10.1016/j.ijfatigue.2019.105191.
[11] Trudel A, Lévesque M, Brochu M. Microstructural effects on the fatigue crack growth resistance of a stainless steel CA6NM weld. Eng Fract Mech 2014;115:60–72. http://dx.doi.org/10.1016/j.engfracmech.2013.11.013.
[12] Igwemezie V, Mehmanparast A, Brennan F. The influence of microstructure on the fatigue crack growth rate in marine steels in the Paris region. FFEMS 2020;43(10):2416–40. http://dx.doi.org/10.1111/ffe.13312.
[13] Dowse K, Richards C. Fatigue crack propagation through weld heat affected zones. Met Trans 1971;2(2):599–603. http://dx.doi.org/10.1007/BF02663355.
[14] Richards C, Lindley T. The influence of stress intensity and microstructure on fatigue crack propagation in ferritic materials. Eng Fract Mech 1972;4(4):951–78. http://dx.doi.org/10.1016/0013-7944(72)90028-8.
[15] Suresh S, Ritchie R. A geometric model for fatigue crack closure induced by fracture surface roughness. Met Trans A 1982;13(9):1627–31. http://dx.doi.org/10.1007/BF02644803.
[16] Jayaprakash M, Mustapa SM, Mutoh Y, Sadasue T. Effect of microstructure on fatigue crack growth behavior of structural steel. In: The proceedings of the materials and processing conference 2007.15. JSME; 2007, p. 161–2. http://dx.doi.org/10.1299/jsmemp.2007.15.161.
[17] BSI. Guide to methods for assessing the acceptability of flaws in metallic structures. Br Stand Inst 2015. BS 7910:2013+A1:2015.
[18] Ito Y, Komizo Y-i, Nakanishi M. Carbon equivalent and hardness for cracking tendency of C-mn microalloyed structural steel. IIW; 1985.
[19] ABAQUS/Standard user's manual, version 6.14. United States: Dassault Systèmes Simulia Corp; 2009.
[20] Brandis H. Rechnerische bestimmung der umwandlungstemperaturen von niedriglegierten staehlen. CNRS 1975.
[21] ESI Group. SYSWELD: Welding and heat-treatment simulation software. 2007, Finite-element software for coupled thermal, metallurgical, and mechanical welding simulation. Computer software, version 8.10.
[22] Loose T. Einfluß des transienten schweißvorganges auf verzug, eigenspannungen und stabilitätsverhalten axial gedrückter kreiszylinderschalen aus stahl [Ph.D. thesis], Karlsruhe, Univ., Diss.; 2007, 2007.
[23] ASTM. Standard test method for measurement of fatigue crack growth rates. American Society for Testing and Materials; 2024, http://dx.doi.org/10.1520/E0647-23A, ASTM E647-23a.
[24] Leonetti D, Maljaars J, Snijder HB. Fracture mechanics based fatigue life prediction for a weld toe crack under constant and variable amplitude random block loading—Modeling and uncertainty estimation. Eng Fract Mech 2021;242:107487. http://dx.doi.org/10.1016/j.engfracmech.2020.107487.
[25] Janssen M, Zuidema J, Wanhill R. Fracture mechanics: fundamentals and applications. CRC Press; 2004.
[26] ECCS. European database of steel properties (S235 to HSS S460; S550; S690). Tech. rep., ECCS; 2015, SAFEBRICTILE: Standardization of Safety Assessment Procedures across Brittle to Ductile Failure Modes.
[27] Matelect Ltd. ACPD crack growth monitor TYPE CGM7 instruction manual. Harefield, UK: Matelect Ltd.; 2015, URL https://www.matelect.com/files/Download/CGM7v25.pdf. Revision K, accessed from Matelect website.
[28] Bachmann V, Munz D. Fatigue crack closure evaluation with the potential method. Eng Fract Mech 1979;11(1):61–71. http://dx.doi.org/10.1016/0013-7944(79)90030-4.
[29] Hartman GA, Johnson DA. DC electric-potential method applied to thermal/mechanical fatigue crack growth. Exp Mech 1987;27:106–12. http://dx.doi.org/10.1007/BF02318872.
[30] Forman RG, Mettu SR. Behavior of surface and corner cracks subjected to tensile and bending loads in Ti-6Al-4V alloy. Tech. rep., 1990.
[31] Korda AA, Miyashita Y, Mutoh Y, Sadasue T. Fatigue crack growth behavior in ferritic–pearlitic steels with networked and distributed pearlite structures. Int J Fatigue 2007;29(6):1140–8. http://dx.doi.org/10.1016/j.ijfatigue.2006.09.008.
[32] Mustapa MS, Mutoh Y. Effects of size and spacing of uniformly distributed pearlite particles on fatigue crack growth behavior of ferrite–pearlite steels. Mater Sci Eng A 2010;527(10–11):2592–7. http://dx.doi.org/10.1016/j.msea.2009.12.023.
[33] Mustapa MS, Mutoh Y. Effect of hardness of second phase particle on fatigue crack growth behavior of steels with hard second phase particle in soft ferrite matrix. Adv Mater Res 2010;129:775–9. http://dx.doi.org/10.4028/www.scientific.net/AMR.129-131.775.
[34] Dickson JI, Baïlon J-P, Masounave J. A review on the threshold stress intensity range for fatigue crack propagation. Can Metall Q 1981;20(3):317–29. http://dx.doi.org/10.1179/cmq.1981.20.3.317.
[35] Wasen J, Hamberg K, Karlsson B. The influence of grain size and fracture surface geometry on the near-threshold fatigue crack growth in ferritic steels. Mater Sci Eng: A 1988;102(2):217–26.
[36] Wilson D, Dunne FP. A mechanistic modelling methodology for microstructure-sensitive fatigue crack growth. J Mech Phys Solids 2019;124:827–48. http://dx.doi.org/10.1016/j.jmps.2018.11.023.
[37] Elber W, et al. The significance of fatigue crack closure. 1971.
[38] Zerbst U. Application of fracture mechanics to welds with crack origin at the weld toe—a review. Part 2: welding residual stresses. Residual and total life assessment. Weld World 2020;64(1):151–69. http://dx.doi.org/10.1007/s40194-019-00816-y.
[39] Gray GT, Williams J, Thompson A. Roughness-induced crack closure: an explanation for microstructurally sensitive fatigue crack growth. Met Trans A 1983;14(2):421–33. http://dx.doi.org/10.1007/BF02644220.
[40] Malschaert D, Veljkovic M, Maljaars J. Numerical simulations of residual stress formation and its effect on fatigue crack propagation in a fillet welded T-joint. Eng Fract Mech 2024;110236.
[41] Bowness D, Lee MM. Fracture mechanics assessment of fatigue cracks in offshore tubular structures. 2002.
[42] CEN. Eurocode 3: Design of steel structures - part 1-9: Fatigue. European Committee for Standardization; 2025.
[43] Carpinteri A, Brighenti R. Part-through cracks in round bars under cyclic combined axial and bending loading. Int J Fatigue 1996;18(1):33–9. http://dx.doi.org/10.1016/0142-1123(95)00076-3.
[44] Pucillo GP, Esposito L, Leonetti D. On the effects of unilateral boundary conditions on the crack growth rate under cycling bending loads. Int J Fatigue 2019;124:245–52. http://dx.doi.org/10.1016/j.ijfatigue.2019.02.038.
[45] Pang JH, Tsang KS, Hoh HJ. 3D stress intensity factors for weld toe semi-elliptical surface cracks using XFEM. Mar Struct 2016;48:1–14. http://dx.doi.org/10.1016/j.marstruc.2016.04.001.